

BIOCHEMICAL AND ELECTROPHYSIOLOGICAL MODIFICATION OF AMYLOID TRANSTHYRETIN ON CARDIOMYOCYTES

Running title: Cardiomyocyte effects of TTR aggregates

L. Sartiani^{1,2*}, M. Bucciantini^{3,4*}, V. Spinelli^{1,2}, M. Leri³, A. Natalello⁵, D. Nosi⁶, S. Doglia⁵, A. Relini⁷, A. Penco⁷, S. Giorgetti⁸, E. Gerace⁹, G. Mannaioni¹, V. Bellotti^{8,10}, S. Rigacci³, E. Cerbai^{1,2,4} & M. Stefani^{3,4}

¹Department of Neuroscience, Psychology, Drug Research and Child Health (NeuroFarBa), University of Florence, Florence, Italy; ²Center of Molecular Medicine (C.I.M.M.B.A.), University of Florence Florence, Italy; ³Department of Biomedical, Experimental and Clinical Sciences “Mario Serio”, University of Florence, Florence, Italy; ⁴Research Centre on the Molecular Basis of Neurodegeneration, University of Florence, Florence, Italy; ⁵Department of Biotechnology and Biosciences, University of Milan - Bicocca, Milan, Italy and the National Inter-University Consortium for the Physical Sciences of Matter (CNISM), RU Milano - Bicocca, Milan, Italy; ⁶Department of Experimental and Clinical Medicine, University of Florence, Florence, Italy; ⁷Department of Physics, University of Genoa, Genoa, Italy; ⁸Department of Molecular Medicine, Institute of Biochemistry, University of Pavia, Pavia, Italy.; ⁹Department of Health Science, University of Florence, Florence, Italy ¹⁰Wolfson Drug Discovery Unit, Centre for Amyloidosis and Acute Phase Proteins, Division of Medicine, University College London, London, United Kingdom.

* Equal contribution

Corresponding author

Elisabetta Cerbai, PhD
Department of NeuroFarBa
C.I.M.M.B.A.
University of Florence
Viale Pieraccini, 6
50139 Florence (Italy)
Tel.: +39 055 4271247
Fax: + 39 055 4271280
e-mail: elisabetta.cerbai@unifi.it

Abstract

Transthyretin (TTR) amyloidoses are familial or sporadic degenerative conditions often with heavy cardiac involvement. Presently, effective pharmacological therapy for TTR amyloidoses is not available mostly due to the substantial lack of knowledge on both the molecular mechanisms of TTR aggregation in tissue and the ensuing functional and viability modifications in aggregate-exposed cells. TTR amyloidoses are of particular interest for the relation between functional and viability impairment in aggregate-exposed excitable cells, such as peripheral neurons and cardiomyocytes. In particular, the latter cells provide the opportunity to investigate in parallel the electrophysiological and biochemical modifications when exposed for varying lengths of time to variously aggregated wtTTR, a condition that characterizes senile systemic amyloidosis (SSA).

In this study we investigated biochemical and electrophysiological modifications in cardiomyocytes exposed to amyloid oligomers or fibrils of wtTTR or to its T4-stabilized form, which resists tetramer disassembly, misfolding and aggregation. The amyloid TTR cytotoxicity results in mitochondrial potential modification, oxidative stress, deregulation of cytoplasmic Ca^{2+} levels and Ca^{2+} cycling. The altered intracellular Ca^{2+} cycling causes a prolongation of the action potential performed by whole-cell recordings of action potential on isolated mouse ventricular myocytes which may contribute to the development of cellular arrhythmias and conduction alterations often seen in patients with TTR amyloidosis.

Our data add information on the biochemical, functional and viability alterations in cardiomyocytes exposed to aggregated TTR providing clues on the molecular and physiological basis of heart dysfunction in sporadic (SSA) and familial (FAC) forms of TTR amyloidoses.

Abbreviations

AFM: Atomic Force Microscopy

FT-IR: Fourier transform infrared

CR: Congo Red

CTX-B: Cholera toxin B subunit

MTT: 3-(4, 5-dimethylthiazol-2-yl)-2,5-diphenyltetrazolium bromide

GM1: monosialotetrahexosylganglioside

2-APB: 2-aminoethyl diphenylborinate

Introduction

In the past years, misfolded proteins have been proposed to play a key role in the pathophysiology of several cardiac diseases in humans, including pathologic cardiac hypertrophy, dilated and ischemic cardiomyopathy. Actually, cardiac stress disorders, including dilated and hypertrophic cardiomyopathies are associated with the presence of soluble protein oligomers in cardiomyocytes (1). These data have led to suggest that protein misfolding and the ensuing proteotoxicity are important contributors to the establishment and progression of heart failure, and to parallel cardiac dysfunction as Alzheimer's disease of the heart (2). Such knowledge has consolidated the idea that targeting the accumulation of misfolded proteins can be beneficial in patients with heart failure.

Actually, several systemic amyloidosis display congestive heart failure and a variety of alterations in cardiac electrogenesis and conduction that contribute considerably to disease-associated morbidity and mortality (3, 4). Human transthyretin (TTR) is one of the proteins whose amyloid aggregates are often associated with heart disease. TTR is a 55 kD homotetramer synthesized by the liver and the choroid plexus, which carries T4 and the retinol-binding protein in the plasma and cerebrospinal fluid (5). Extracellular aggregates of wild type TTR (wtTTR) are found in senile systemic amyloidosis (SSA), a condition affecting around 25% of the population over 80 years; a more severe phenotype characterizes familial amyloid cardiomyopathy (FAC), where TTR aggregation occurs as a consequence of any out of a number of described mutations in the TTR gene (6,7). Presently, an effective therapy against TTR amyloidosis is still lacking, and the most severe cases of SSA and FAC can be treated only by liver and, when the case, heart transplantation. Correspondingly, the molecular and functional mechanisms underlying wtTTR aggregation and toxicity in cardiac tissue remain ill-defined.

Amyloid aggregation of TTR is preceded by tetramer destabilization into monomers/dimers with exposed hydrophobic surface and monomer/dimer misfolding, which results in structural reorganization into amyloid assemblies (8, 9). Most of the known TTR mutations in humans have been shown to be amyloidogenic favoring tetramer destabilization (10), whereas tetramer stabilization, as it occurs in some mutants such as the stable and non-amyloidogenic Thr119Met as well as following T4 binding, slows down the rate of dissociation of TTR tetramer, thus hindering fibril growth (11). The identity of the cytotoxic species associated with amyloid disease and in TTR amyloidosis is far from clear despite a plethora of studies in recent years. Several studies indicate that usually fibril deposition into amyloid aggregates is preceded by the appearance of toxic low molecular weight oligomeric aggregation nuclei (12,13) which impair cell viability notably by altering intracellular ion homeostasis (14-16), even though cell sufferance caused by nutrient shortage due to the physical barrier represented by the fibrillar burden can play an important role as well (17). Accordingly, TTR fibrils, previously considered direct responsible of tissue impairment in FAP/FAC and SSA, are now thought to be by far less toxic than their unstable oligomeric precursors that, presently, are considered the main responsible of cell damage and tissue functional impairment (18). Actually, it has long been thought that the mass of deposited amyloid fibrils was the sole responsible for tissue dysfunction. However, inflammation, apoptosis and ROS markers characteristic of tissue damage can be detected in human carriers of mutant TTR well before amyloid deposit appearance. These markers have been associated with amorphous TTR aggregates that can be observed in the early stages of disease evolution (18). Nevertheless, there is a substantial body of experimental evidence that fully demonstrates that amyloid fibrils are capable of causing cellular death in numerous situations (19-29). This raises the possibility that the molecular determinants underlying aggregate cytotoxicity may not always be associated with the same type of species, and that there can well be oligomers and fibrils with different structural and biophysical properties and hence with different abilities to interact with, disassemble, permeabilize and deregulate the cell membrane (30). Presently, very reduced information is available on the biochemical and cell modifications occurring in cardiomyocytes (CMs) exposed to aggregated TTR (32), whereas valuable knowledge does exist on the biochemical alterations and the occurrence of specific functional (e.g. electrophysiological) abnormalities resulting from exposure to toxic TTR amyloids of neuronal cells, with ensuing Ca^{2+} influx via TRPM8 and NaV1.8 channels (14). Furthermore, the possible involvement in these modifications of specific lipid clusters was inferred on the basis of some perturbation of Ca^{2+} conductance (15). Both mechanisms are of potential relevance in CMs.

In this study, we used HL-1 and primary mouse CM cultures exposed to aggregated wtTTR to investigate the features of aggregate-cell interaction and the ensuing electrophysiological and biochemical modifications resulting in cell functional and viability impairment. In particular, after a careful biophysical characterization of TTR aggregation *in vitro*, we investigated some electrophysiological alterations following cell exposure to TTR aggregates that recapitulate, *in vitro*, specific and crucial aspects of SSA in order to gather into a whole picture data on cell biochemical, functional and viability impairment provided by wtTTR at different stages of aggregation. As far as we know, our findings are the first reported on the biochemical and electrophysiological modifications occurring in CMs exposed to amyloid aggregates of wtTTR. Our data provide novel insights into the molecular and functional basis of heart pathophysiology in TTR amyloidosis.

Material and Methods

wtTTR production

Recombinant wtTTR was produced in a bacterial expression system using the *E. coli* BL21B DE3 (pLysS) strain. The expressed protein was purified by gel-filtration and ion exchange chromatography and its purity was checked by Agarose Gel and SDS PAGE. Native, T4-stabilized wtTTR (TTR-T4) was obtained by adding T4 to the wtTTR solution. Briefly, T4 was dissolved in DMSO (Sigma-Aldrich Saint Louis, MO, US) at 1.0 mM concentration for 1 h at room temperature; then the solution was diluted in PBS containing wtTTR to a TTR:T4 ratio of 1:2. TTR oligomers (TTR-ol) and fibrils (TTR-fib) were generated by TTR incubation in 100 mM acetate buffer, pH 4.4 at 25 °C for 24 h or 96 h, respectively. In all experiments, aggregate concentration was expressed as soluble tetramer concentration.

Congo Red (CR) assay and Fourier Transform- Infrared (FT-IR) analysis

Fibril growth was followed by CR assay and FT-IR analysis. The former was performed by mixing 133 μ L of the protein solutions with 867 μ L of a 10 mM phosphate buffer, pH 7.4, solution containing 20 μ M CR and 150 mM NaCl. Solutions without protein or without CR were also prepared as controls. The CR absorption spectra were acquired after 2-3 min equilibration using an Ultrospec 2000 spectrophotometer (Pharmacia Biotech).

The FT-IR spectra were collected in attenuated total reflection (ATR) on a protein hydrated film by a standardized approach (33, 34). Briefly, 3.0 μ L sample aliquots were deposited on the single reflection diamond plate of the Golden Gate ATR device (Specac, USA) and the spectra were collected after solvent evaporation. The 670-IR spectrometer (Varian Australia Pty Ltd., Mulgrave VIC, AU) equipped with a nitrogen-cooled Mercury Cadmium Telluride detector and an air dryer purging system, was used under the following conditions: 2.0 cm^{-1} spectral resolution, 25 kHz scan speed, 1000 scan co-additions, and triangular apodization. The second derivatives of the measured spectra were obtained by the Savitsky-Golay method using the Resolutions-Pro software (Varian Australia Pty Ltd., Mulgrave VIC, AU). The FT-IR spectrum of soluble TTR was collected at 40 μ M protein concentration in 30 mM sodium phosphate buffer, pH 7.4. For aggregation studies, the TTR spectra were recorded at 20 μ M protein concentration in 100 mM acetate buffer, pH 4.4.

Dynamic Light Scattering (DLS) analysis

Size distributions of the protein samples by volume were obtained after sample centrifugation (18,000 rpm for 10 min). The data were achieved by a Zetasizer Nano S DLS device (Malvern Instruments, Worcestershire, UK) using low volume disposable cells (12.5 \times 45 mm). The temperature was maintained at 25 °C by a thermostated system. The acetate buffer was filtered immediately before use to clean off any impurity.

Atomic Force Microscopy (AFM) and Transmission Electron Microscopy (TEM) analysis of TTR aggregates

For AFM inspection, a 10 μ L aliquot of the sample was deposited on a freshly cleaved mica substrate and dried under mild vacuum. The AFM images were acquired in tapping mode in air using a Dimension 3100 SPM equipped with a 'G' scanning head (maximum scan size 100 μ m) and driven by a Nanoscope IIIa controller, or a Multimode SPM equipped with "E" scanning head (maximum scan size 10 μ m) and driven by a Nanoscope IV controller (Digital Instruments-Bruker, Karlsruhe, Germany). Single beam uncoated silicon cantilevers (type OMCL-AC160TS, Olympus, Tokyo, Japan) were used. The drive frequency was in the 290-330 kHz range; the scan rate was in the 0.5-1.0 Hz range.

For TEM analysis, sample aliquots were withdrawn from the aggregation mixture at regular time intervals to monitor the assembly process following adsorption onto formvar/carbon-coated 400 mesh nickel grids (Agar Scientific, Stansted, UK) and negative staining with 2.0% (w/v) uranyl acetate (Sigma-Aldrich Saint Louis, MO, US). The grids were observed at a 15-30000 \times magnification in a JEM 1010 transmission electron microscope at 80 kV excitation voltage.

Dot blot assay

5.0 μ L samples of 10 μ M wtTTR were spotted onto a nitrocellulose membrane and left to dry. Then the membrane was blocked with 3.0% BSA, 0.1% Tween-20 in TBS (50 mM Tris-HCl buffer, pH 7.5, 150 mM NaCl) for 1.0 h at room temperature, and incubated overnight at 4.0 °C with rabbit anti-TTR polyclonal antibodies (1:2000) and with conformation specific antibodies: the rabbit anti-oligomer (A11) (1:10000) or the rabbit anti-fibril (OC) (1:5000) polyclonal antibody. After three washes in TBS/0.1% Tween-20, the membrane was incubated for 1.0 h at room temperature with peroxidase-conjugated anti-rabbit or anti-mouse antibodies (1:10.000). After three washes in TBS/0.5% Tween-20, the immunodetection was performed with the SuperSignal® West Pico chemiluminescent substrate and Kodak® Biomax MS film.

HL-1 cardiomyocyte and human dermal fibroblast (HDF) cell culture

HL-1 cardiomyocytes were obtained from Dr W. C. Claycomb (Louisiana State University) and grown in T25, gelatin/fibronectin-coated flasks, as previously described (35). The cells were maintained in Claycomb Medium (JRH

Biosciences), supplemented with 10% fetal bovine serum (Life Technologies Italia fil., Monza – MB, Italy), 2.0 mM L-glutamine (Life Technologies Italia fil., Monza – MB, Italy), 0.1 mM noradrenaline (Sigma-Aldrich Saint Louis, MO, US) and 100 U/mL penicillin-streptomycin (Life Technologies Italia fil., Monza – MB, Italy). At confluence, the cells were detached and re-plated at a 1:3 dilution in a new T25 flask or in 96 well plates and used for experimental measurements. HDF cells were cultured at 37°C with in complete medium (DMEM, 10% fetal bovine serum, 3.0 mM glutamine, 100 units/ml penicillin and 100 µg/ml streptomycin), in a humidified, 5.0% CO₂ incubator. Every three days the cells (70-90% confluent) were detached and re-plated at a 1:3 dilution in a new plate or in 96 well plates and used for measurements.

Isolation of mouse ventricular myocytes

Left ventricular cardiomyocytes were isolated from adult C57/6BL mice (Charles River, Wilmington, Massachusetts, US) by enzymatic digestion. Briefly, after heparin injection (5.000 U/mL) and anesthesia with isoflurane, the heart was rapidly excised, mounted on a Langendorff apparatus and perfused with perfusion buffer (see solutions) pre-warmed at 37 °C and equilibrated with 100% O₂. Then, the solution was quickly changed to perfusion buffer plus Liberase DL (0.05 mg/mL, Roche Diagnostics, Indianapolis, US) and CaCl₂ (12.5 µM). The left ventricle was excised, minced, and stirred in perfusion buffer containing CaCl₂ (12.5 µM) and bovine serum albumin (1.0 mg/mL, Sigma-Aldrich Saint Louis, MO, US). The CMs were collected by gravity sedimentation, and stored in Tyrode's solution containing 0.5 mM CaCl₂ and 4.0% penicillin–streptomycin solution, at room temperature. All recordings were completed within 4-6 h from the time of cell isolation.

Calcium imaging

Intracellular Ca²⁺ handling was evaluated as previously reported (36). Briefly, HL-1 and mice ventricular CMs were incubated for 20 min at 37 °C in Tyrode's solution containing 1-5 µL/L fluo-3-acetoxymethyl ester (FLUO-3 AM, Molecular Probes, Eugene, Oregon, US) and 1.0 µL/mL Pluronic F127 solution (Molecular Probes, Eugene, Oregon, US) for dye loading. The preparation was set in the stage of a fluorescence microscope (Leica DMIRE2) properly equipped for fluorescence signal production and detection. Fluo-3 was excited with the light of a xenon lamp (LPS 220; Photo Technology International), using a bandpass filter set at 480±15 nm. Fluo-3 fluorescence was detected at 540±15 nm. Ca²⁺ release from sarcoplasmic reticulum stores was studied using 5.0 µM ryanodine (Tocris Bioscience Missouri, US) or 5.0 µM 2-aminoethyl diphenylborinate (2-APB) (Sigma-Aldrich Saint Louis, MO, US), to block ryanodine and IP3 receptors, respectively. Cardiomyocytes were pre-incubated with the inhibitors for 15 min before recordings. Experimental control of fluorescence acquisition was performed using the software Imaging Workbench (INDEC BioSystems). Data analysis was carried out using the Axon Imaging Workbench program (v2.2.1; Axon Instruments) or Metafluor (Molecular Devices, Sunnyvale, CA, US). Ca²⁺ cumulative content was evaluated in HL-1 CMs as integrated area under the curve after 20 min exposure to experimental condition and reported as mean fractional variation (±s.e.m) with respect to vehicle. Ventricular CMs were paced at 1.0 Hz 1-5 V (pulse duration 1.0 ms) and the Ca²⁺ transients were analyzed to calculate amplitude, baseline level, time to peak, 50% and 90% decay times. The data were reported as mean fractional variation (±s.e.m) relative to the initial values measured for individual cells.

Patch-clamp recordings

Electrophysiological recordings were performed as previously reported (37). The cells were placed in a thermostatic bath on the platform of an inverted microscope (Nikon Diaphot TMD; Kawasaki, Japan). The patch-clamped cell was superfused by means of a temperature-controlled (36±0.5 °C) microsperfuser, allowing rapid changes of the cell-bathing solution. Action potential recordings were performed using a patch amplifier (Axopatch 200B, Molecular Devices, Sunnyvale, CA, US) in whole-cell configuration (current clamp mode) at 1.0 Hz and the signals were digitized via a DAC–ADC interface (Digidata 1200B, Molecular Devices, Sunnyvale, CA, US), acquired by means of pClamp software (version 10, Molecular Devices, Sunnyvale, CA, US), and analyzed using Origin 7.5 (GraphPad Software). The patch-clamp pipettes, prepared from glass capillary tubes (Borosilicate GC150T, Harvard App, Saint-Laurent, Canada) by means of a two-stage puller (P-97, Sutter Instrument, California, US), displayed a resistance of 3.5-5.0 MΩ when filled with the internal solution. During the patch-clamp experiments, TTR aggregates were supplemented to the internal pipette solutions.

Solutions for calcium imaging and electrophysiology

Perfusion buffer (mM): NaCl 113, KCl 4.7, KH₂PO₄ 0.6, Na₂PO₄ 0.6, MgSO₄ 1.2, NaHCO₃ 12, KHCO₃ 10, HEPES 10, Taurine 30, BDM 10, D-(+)-glucose 10, pH 7.30.

Tyrode's solution (mM): D-(+)-glucose 10, Hepes 5.0, NaCl 140, KCl 5.4, MgCl₂ 1.2, CaCl₂ 0.0125, pH 7.3.

Pipette solution (mM): K-Aspartate 130, Na₂-ATP 5, MgCl₂ 2.0, CaCl₂ 5.0, EGTA 11, HEPES-KOH 10, pH 7.2,

Reactive oxygen species (ROS) measurement

Intracellular ROS levels were determined using the fluorescent probe 2',7'-dichlorofluorescein diacetate, acetyl ester (CM-H₂ DCFDA)(Thermo Fisher Scientific, Molecular Probes Waltham, MA USA). CM-H₂ DCFDA is a cell-permeant indicator for ROS that becomes fluorescent upon removal of the acetate groups by intracellular esterases and subsequent oxidation. The latter modification can be detected by monitoring the increase in fluorescence at 538 nm. The HL-1 cells were plated at a density of 10000 cells per well on 96-well plates. After 24 h of cell exposure to the aggregates (10 μ M TTR monomer concentration), 10 μ M DCFDA in DMEM without phenol red was added. After 30 min the fluorescence values at 538 nm were detected by Fluoroscan Ascent FL (Thermo Fisher Scientific, Molecular Probes Waltham, MA USA).

Cell viability assay

The cytotoxicity of the different forms of soluble or aggregated TTR was assessed by the MTT reduction inhibition assay. Briefly, the cells were plated at a density of 1500 cells/well on 96-well plates in 100 μ L culture medium. After 48 h, the medium was changed with 100 μ L of fresh medium containing the different TTR aggregates (10 μ M monomer concentration) or with an equal volume of aggregation buffer (control cells). After 24 h, the cells were incubated for 2.0 h with 100 μ L of serum-free DMEM without phenol red, containing 0.5 mg/mL MTT. Finally, 100 μ L of cell lysis solution (20% SDS, 50% N, N-dimethylformamide) was added to each well; after sample incubation at 37 °C to allow complete lysis, the blue formazan absorbance was read at 570 nm with an automatic plate reader (Bio-Rad). Cell apoptosis was detected by the Annexin V-FITC Apoptosis detection kit (Sigma-Aldrich). A propidium iodide (PI) solution with Annexin V-FITC was used to discriminate among viable, apoptotic and secondary necrotic cells. Briefly, after a 24 h treatment with the TTR aggregates, the cells were incubated with Annexin V-FITC and PI for 10 min, at room temperature. Then the cells were analysed by flow cytometry, Cell viability was determined also using the trypan blue exclusion method. HL-1 cells were treated with TTR aggregates, after 24 h centrifuged at 200 \times g and incubated in 0.2% trypan blue (Sigma, St. Louis, MO) for 10 min at 37°C. Cells were then washed in PBS and counted under phase-contrast microscopy. In this assay, blue cells were concluded to have lost membrane integrity and were scored as nonviable. All counts were performed in triplicate.

Sialic acid cleavage and quantification.

The sialic acid moiety was removed from gangliosides as previously reported (38). Briefly, the cells were starved by incubation with DMEM serum-free media for 3.0 h at 37 °C and then left standing for 2.0 h in the presence of a mixture of neuraminidases from *V. cholerae* (11,7 mU) and *C. perfringens* (100 mU) (Sigma Aldrich Saint Louis, MO, US). The removed sialic acid was measured enzymatically by a specific kit (Roche Molecular Biochemicals Mannheim Germany) according to the manufacturer's instruction.

Mitochondrial membrane potential in living cells

The change of the mitochondrial membrane potential ($\Delta\Psi_M$) in TTR-exposed cells (10 μ M TTR monomer concentration) was detected by a fluorescence-based assay. The cells were cultured for 10 min at 37 °C on coverslips in Dulbecco's modified Eagle's medium containing 5.0 mg/mL of the lipophilic cationic probe (fluorochrome(5,5,6,6-tetrachloro-1,1,3,3-tetraethylbenzimidazolcarbocyanine iodide) (JC-1 stain, Thermo Fisher Scientific, Waltham, MA USA). At hyperpolarized mitochondrial membrane potential (-140 mV), this dye forms a red fluorescent J-aggregate, whereas at depolarized membrane potential (-100 mV) it remains in the green fluorescent monomeric form. Prior to detection, the cells were washed in PBS and placed in an open slide-flow loading chamber mounted on the stage of a confocal scanning microscope (Bio-Rad) equipped with a krypton/argon laser source. The emitted fluorescence was monitored at 488 nm and 568 nm with a Nikon plan ApoX60 oil-immersion objective. Series of optical sections (512 \times 512 pixels) were taken through the depth of the cells with a thickness of 1.0 μ m at intervals of 0.8 μ m. Twenty optical sections for each sample were projected as a single composite image by superimposition.

Confocal immunofluorescence

Sub-confluent HL-1 cells grown on glass coverslips were exposed to 10 μ M TTR aggregates (monomer concentration) for 24 h. After incubation, the cells were washed with PBS and fixed in 2.0% buffered paraformaldehyde for 10 min. Then, the cells were counterstained with 50 μ g/mL tetramethylrhodamine-conjugated wheat germ agglutinin (WGA) (Thermo Fisher Scientific, Molecular Probes Waltham, MA USA) for 45 min at room temperature, permeabilized by treatment with acetone at -20 °C for 1.0 min, washed with PBS and blocked with PBS containing 0.5% BSA and 0.2% gelatin. After counterstaining, the cells were incubated for 1.0 h at room temperature with an anti-TTR rabbit polyclonal antibody or with an anti-oligomer rabbit polyclonal antibody (A11) diluted 1:1000 and 1:10,000, respectively, in the blocking solution and then washed with PBS for 30 min under stirring. The immune reaction was revealed by Alexa488 or Alexa568-conjugated anti-rabbit secondary antibody (Thermo Fisher Scientific, Molecular Probes Waltham, MA USA) diluted 1:400 in PBS. Finally, the cells were washed twice in PBS and once in redistilled water to remove any non-specifically bound antibody.

Cell surface GM1 labeling was performed by incubating the cells with 10 ng/mL Alexa488-conjugated cholera toxin B (CTX-B) in complete medium for 20 min at room temperature. Cell fluorescence was imaged using a confocal Leica TCS SP5 scanning microscope (Leica, Mannheim, Ge) equipped with a HeNe/Ar laser source for fluorescence measurements. The observations were performed using a Leica Plan Apo X63 oil immersion objective, suited with optics for DIC acquisition. Series of 0.5 μ m thick optical sections (1024 \times 1024 pixels) were taken through the cell depth at 0.4 μ m intervals and 20 optical sections for each examined sample were Z-projected. To quantify the immunofluorescence intensity of cell-associated TTR we randomly selected ten fields of view from three separate experiments. Co-localization analysis was performed by using developed algorithms such as the overlap coefficient according to Manders and the co-localization coefficients k_1 and k_2

$$R = \frac{\sum_i S1_i \cdot S2_i}{\sqrt{\sum_i (S1_i)^2 \cdot \sum_i (S2_i)^2}} \quad k_1 = \frac{\sum_i S1_i \cdot S2_i}{\sum_i (S1_i)^2} \quad k_2 = \frac{\sum_i S1_i \cdot S2_i}{\sum_i (S2_i)^2}$$

where S1 and S2 represent signal intensity of pixels in the channel 1 and 2, respectively.

Data analysis and Statistics

Statistical analysis was performed by means of Prism program (Graph Pad Software, U.S.A.) using the Student's *t* test for grouped data or ANOVA followed by the Tukey's multiple comparison test for all other values. A probability value < 0.05 was considered significant.

Results

Morphological analysis and biophysical properties of wtTTR aggregates

The wtTTR assemblies TTR-T4, TTR-ol and TTR-fib grown at pH 4.4 at differing incubation times were first characterized by spectroscopic and morphological analysis. The conformational properties of TTR-T4 and aggregated TTR were initially investigated at pH 7.4 by FT-IR spectroscopy, which allows studying protein secondary structure and aggregation by the analysis of the IR absorption spectrum in the Amide I region (1700-1600 cm^{-1}). TTR-T4 displayed the Amide I maximum around 1630 cm^{-1} (Fig. 1A), a signal resulting from the intramolecular β -sheet structure of the native protein (28). The second derivative of the spectrum (Fig. 1B) disclosed additional components at \sim 1691 cm^{-1} , \sim 1675 cm^{-1} , and \sim 1649 cm^{-1} , that can be assigned to β -sheets, turns/ β -sheets, and α -helical/random coil structures, respectively. At pH 4.4, wtTTR fibrillized. At these conditions, after \sim 3 min the peak at 1630 cm^{-1} assigned to the intramolecular β -sheet component slightly decreased in intensity and shifted to higher wavenumbers (Fig. 1A and 1B), suggesting partial unfolding/misfolding of TTR secondary structures, as reported for other proteins (33, 39). Prolonged incubation at pH 4.4 resulted in the appearance of a downshift of the main β -sheet component indicating some rearrangement of the β -sheet contacts in the growing aggregates. After 96 h of incubation, the TTR spectrum displayed both a narrower Amide I band, as compared to that of the natively folded protein, whose maximum down-shifted to \sim 1624 cm^{-1} and a new well resolved component at \sim 1692 cm^{-1} , characteristic of intermolecular β -sheets in amyloid fibrils (40, 41). These modifications of the FT-IR spectra of wtTTR were not found at pH 7.4, where the spectra collected at different times of incubation were almost superimposable to that at T_0 without apparent changes (Fig. 1C), and indicating protein stability. The different behavior of wtTTR at pH 4.4 and pH 7.4 were more evident when peak position of the main β -sheet component was plotted against time (Fig. 1D); the plot was sharply modified only at the acidic pH.

In the first 24 h of TTR incubation at pH 4.4, AFM and TEM imaging (Fig. 2A and 2B) showed the presence of differently-sized oligomeric structures (TTR-ol) 2.7 \pm 0.1 nm in height coexisting with short, worm-like prefibrillar assemblies of 3.5 \pm 0.1 nm in height. These protofibrils displayed a nodular morphology, resembling short chains of beads. Amyloid fibrils (TTR-fib) were not present at this aggregation time. Fibrils 5.7 \pm 0.1 nm in height appeared later, after 96 h of protein incubation.

The transition from natively folded to oligomeric TTR was also investigated by DLS. An apparent hydrodynamic diameter ($D_{h,app}$) of about 7.0 nm was found for TTR-T4, which was consistent with its tetrameric structure (Fig. 2E) (42). However, following wtTTR incubation for 24h at acidic pH, larger oligomeric forms with a $D_{h,app}$ of about 1000 nm appeared, which became prevalent with increasing time (Fig. 2E).

To better investigate the nature of the oligomeric and fibrillar structures grown at these conditions, the aggregated TTR samples were analyzed by immunoblotting using the oligomer-specific A11 and the fibril-specific OC antibody. The A11 antibody immunostained both TTR-ol and, to a lesser extent, TTR-fib sample while only TTR-fib showed a significant OC-immunoreactivity. In contrast, TTR-T4 did not exhibit any immunoreactivity either A11 or OC antibodies (Fig. 2C). The amyloid nature of TTR-ol and TTR-fib was further confirmed by the red-shift of the CR absorbance maximum, a signature of the amyloid fold (Fig. 2D). The shift was not observed in the TTR-T4 incubated at the same conditions (data not shown).

Immunolocalization of TTR aggregates

After having described the structural features of TTR, both natively folded (TTR-T4) and under aggregating conditions (TTR-ol, TTR-fib), we sought to determine whether these different TTR species were able to interact with the plasma membrane of cultured HL-1 cells and the extent of the interaction. When the cells were exposed to the stabilized TTR-T4, we failed to detect any protein interaction with the cell membrane (Fig.3A), in agreement with recently reported data relative to the non-amyloidogenic, stabilized T119M variant (32); however, a significant association of TTR aggregates to cell surface was seen in HL-1 cells treated with TTR-ol or TTR-fib (Fig. 3B and 3C). Contrary to TTR-fib, TTR-ol was also found to be significantly internalized into these cells after 24 h exposure as shown by a representative magnified Y projection of a cell: TTR-fib was only observed in contact with the outer surface of the cell membrane (Fig. 3E) whereas TTR-ol was found in the cytoplasm as A11 immunopositive punctate fluorescence (Fig. 3D). The oligomers and fibrils association with cell membrane was evident (to a less extent for the fibril sample) also on human dermal fibroblast HDF \square as shown in Fig. S1 suggesting that TTR aggregates did not exhibit a distinct cellular specificity. However, in these cells was not evident any internalization of oligomeric species (Fig. S1).

The role of the monosialoganglioside GM1, a major raft marker, in promoting aggregate-membrane interaction was also investigated. In fact, besides favoring peptide/protein misfolding and aggregation, recent data indicate that GM1 can also mediate the interaction of amyloid assemblies with the plasma membrane, notably by its negatively charged sialic acid component (27). Therefore, to further elucidate whether our TTR aggregates did interact with the cell membrane at GM1-rich sites and the role of the negatively charged sialic acid moiety of GM1, we carried out confocal fluorescence microscopy experiments using a polyclonal antibody raised against wtTTR; the cell membrane was counterstained by Alexa 488-conjugated CTX-B, a fluorescent probe that binds predominantly GM1 on the cell membrane. In some experiments, the cells were treated with a mixture of neuraminidases (NAM) to specifically cleave sialic acid residues from the cell surface prior to aggregate exposure. Such treatment is milder respect to reducing membrane GM1 by treating cells with fumonisin or other inhibitors of GM1 synthesis since it maintains the GM1 backbone inside the bilayer and therefore does not perturb membrane lipid order. The treatment caused a significant decline (about 2.5-fold) of the sialic acid on HL-1 cells, as shown in Fig. 3H, without affecting cell viability (data not shown). At these conditions, we found that the signal of both TTR-ol and TTR-fib on the cell membrane was significantly reduced in NAM-treated cells (Fig.3F, 3G and 3I). The co-localization analysis by the Overlap Coefficient did not show significant differences between NAM-treated and NAM-untreated samples (Table. 1). Therefore, the ratio between the overlap coefficients k1 (weighted overlap of TTR immunofluorescence, red, to GM1 fluorescence) and k2 (weighted overlap of GM1 fluorescence, green, to TTR immunofluorescence) was used to determine the degree of GM1 recruitment in the co-localization areas (42). The analysis showed that in the cells treated with TTR-fib the k1/k2 ratio was lower than in the cells treated with TTR-ol, suggesting that TTR fibrils promote higher GM1 recruitment in the co-localization areas. When the cells were treated with NAM, the k1/k2 ratio increased but the total TTR immunofluorescence signal decreased as shown in Fig. 3I indicating that, in NAM-treated cells fibril/membrane interaction and GM1 clustering on the cell membrane are reduced. In conclusion, aggregate recruitment to the cell membrane was deeply dependent on the presence of negatively charged molecules, notably GM1, whose decrease affected much more fibril than oligomer binding.

Taken together, these data confirm that TTR aggregates bind at the cell surface, thus favouring oligomer internalization; they also suggest that the interaction involves GM1 and occurs preferentially at its negatively charged moiety, highlighting the importance of electrostatic binding. Finally, our data agree previous studies indicating that TTR aggregates display high affinity for synthetic lipid membranes rich in anionic phospholipids (44).

Aggregate cytotoxicity

Once established that different wtTTR aggregates bind to membrane sites where sialic acid residues, notably those bound to GM1, are present and that binding is followed by internalization, in the case of oligomers, we tested whether such events modulated cell viability and caused distinct biological effects. Initially, we checked TTR cytotoxicity to HL-1 cells by the MTT reduction assay. As expected, TTR-T4 was harmless to exposed cells (Fig. 4A), similarly to the stabilized T119M mutant (32) whereas TTR-ol and TTR-fib displayed significant cytotoxicity, in agreement with their ability to interact with the plasma membrane (Fig.4A). We also compared the cytotoxic effect of TTR aggregates on HDF \square cells. These cells, despite the presence of aggregate on the membrane, resulted more resistant to amyloid insult (Fig.S1) suggesting a different vulnerability of varying cell types exposed to the same toxic aggregates. The decreased MTT reduction observed in HL-1 cells was not related to apoptotic or necrotic events (data not shown) suggesting that after 24 h of exposure to TTR aggregates the HL-1 cells showed a significant impairment of mitochondrial functionality without cell death or activation of apoptosis. This finding was confirmed by the ROS-sensitive fluorescent probe CM-H2DCFDA; in fact, we found that incubation for 24 h with TTR-ol stimulated ROS production in HL-1 cells and that this effect was enhanced when the cells were exposed to TTR-fib (Fig.4B). We used the JC-1 dye to further confirm whether aggregate cytotoxicity was associated with mitochondria dysfunction, as previously shown for A β aggregates in Alzheimer's disease (, 45). Therefore, we checked by confocal microscopy the effect on the mitochondrial membrane potential ($\Delta\psi_m$)

of HL-1 exposure to TTR-T4 or to variously aged wtTTR aggregates. We found a significant, yet similar, decrease of $\Delta\psi_m$ in cells exposed to TTR-ol or to TTR-fib but not to TTR-T4 (Fig.4C and 4D), as shown by the disappearance of the red fluorescence and/or the increase of the green fluorescence. In particular, some cells were devoid of red fluorescence, which indicates loss of $\Delta\psi_m$ and severity of cell damage. These data indicate that, in HL-1 cells, the cytotoxicity of extracellular TTR oligomers and fibrils proceeds through adsorption to the plasma membrane and results in ROS generation and alteration of the mitochondrial membrane potential.

Effect of TTR aggregates on cytoplasmic calcium levels in HL-1 cardiomyocytes

It has previously been reported that both Ca^{2+} deregulation and ER stress contribute to TTR toxicity to neuronal cells (15, 16). We therefore investigated whether some acute deregulation of cytoplasmic Ca^{2+} levels contributed to the early events following interaction of aggregated wtTTR with the sarcolemma and subsequent oligomer internalization. Typical experimental traces detected in quiescent HL-1 cells (i.e., not exhibiting spontaneous action potentials and associated intracellular Ca^{2+} oscillations) are reported in Fig 5A, which shows a slow, progressive increase of Ca^{2+} levels during acute cell exposure to the same concentration of either TTR-ol (grey trace) or TTR-fib (black trace). At all conditions, the Ca^{2+} concentration was sensitive to caffeine that, as expected, evoked a fast transient Ca^{2+} rise following depletion of sarcoplasmic reticulum (SR) stores. The cumulative Ca^{2+} content was calculated as integrated area under the curve recorded for 20 min and expressed as fractional variation (mean \pm s.e.m, Fig.5B) relative to vehicle. Ca^{2+} increase was statistically significant with respect to vehicle for both TTR-ol and TTR-fib but not for TTR-T4 (see Table S I for a detailed statistical analysis).

Spontaneous calcium oscillations were observed in nearly one third of confluent HL-1 cells exposed to vehicle at 37 °C (Fig. 6A); as previously reported (45,46), oscillations appeared irregular in frequency, amplitude and duration (see inset of Fig. 6A). Estimated oscillations frequency values were 6.3 ± 1.1 beats per minute (bpm) for cells treated with vehicle (n=19), 5.4 ± 2.5 bpm for cells treated with wtTTR (n=14) and 5.9 ± 1.5 bpm for cells treated with TTR-T4 (n=15). Notably, baseline calcium signal remained constant throughout the experimental interval with the vehicle as well as with wtTTR or TTR-T4 (Fig. 6B, K). Interestingly, both TTR-fib and TTR-ol did not produce any gross modification in oscillation frequency values, that were 6.3 ± 1.2 bpm (n=11) and 5.6 ± 1.5 bpm (n=17), respectively; however, similarly to quiescent HL-1 cells, both TTR-fib and TTR-ol clearly induced a net increase of baseline calcium signal, indicating a progressive accumulation of cytosolic calcium (Fig.6C, G).

Considering that the rise of cytosolic Ca^{2+} in oligomer- and fibril-exposed cells resulted from aggregate interaction with the cell membrane and, possibly, oligomer internalization, we hypothesized that in cells exposed to TTR-ol, the internalized species gained access to the Ca^{2+} stores in the SR favoring Ca^{2+} exit to the cytosol, as previously shown for the ER in a mouse neuronal cell line (16). Therefore, we studied whether the Ca^{2+} deposits in HL-1 were sensitive to cell exposure to TTR-ol, TTR-fib and TTR-T4 by investigating the possible involvement of the ryanodine (Rya) and the IP₃-receptors, two well-known SR receptors that regulate Ca^{2+} handling in CMs. HL-1 cells were pre-incubated with ryanodine and 2-APB for 15 min to block ryanodine and IP₃-receptors, respectively, before and during exposure to TTR-ol, TTR-fib or TTR-T4. At these conditions, the rise of intracellular Ca^{2+} was significantly reduced (Fig.5B and Table S I), suggesting an involvement of the ryanodine and IP₃-receptors and hence of the SR Ca^{2+} stores. In automatic HL-1 cells, spontaneous calcium oscillations were eliminated by depletion of intracellular calcium stores with Rya and 2-APB (Fig.6E-N). Nonetheless, during Rya or 2APB treatment, TTR-ol or TTR-fib were still able to produce a modest yet visible raise of the baseline calcium signal (Fig.6E, J), in line with the effect observed in quiescent HL-1 cells (Fig.5B).

It is known that amyloid oligomers permeabilize the plasma membrane of the exposed cells favoring uncontrolled Ca^{2+} entry from the extracellular milieu either non-specifically following disassembly of the membrane bilayer (48,49) and/or through the participation of specific Ca^{2+} channels (50,51). Therefore, we removed Ca^{2+} from the external solution to check whether and to what extent the CM plasma membrane, in addition to the SR one, was involved in intracellular Ca^{2+} rise induced by TTR aggregates. At these conditions, the rise of cytosolic Ca^{2+} in cells exposed to either TTR-ol or TTR-fib was significantly reduced (Fig.5B and Table S I). Spontaneous calcium oscillations were also eliminated in automatic HL-1 cells by removal of external Ca^{2+} (Fig.6D-L), in agreement with previous data (47); similarly to what observed in not automatic HL-1 cells (Fig.5B), exposure to either TTR-fib or TTR-ol enhanced the baseline calcium signal (Fig.6D, H). Thus, Ca^{2+} influx from the extracellular medium and release from the internal stores both contribute to the cytoplasmic Ca^{2+} rise induced by prefibrillar and fibrillar wtTTR.

Effect of TTR aggregates on calcium cycling and action potential profile of mouse ventricular myocytes

The enhanced intracellular Ca^{2+} levels in cells exposed to TTR-ol or TTR-fib led us to hypothesize that the presence of TTR aggregates could alter Ca^{2+} cycling and membrane potential during myocyte contraction. To test this hypothesis we measured Ca^{2+} transients in mice ventricular CMs during contraction evoked by electrical stimulation. As shown in Fig. 7A, cell treatment with 10 μ M TTR-ol increased Ca^{2+} transient amplitude after 5 min (b), 10 min (c) and 15min (d) exposure. At the same times mean fractional variations of Ca^{2+} transient amplitude (Fig.7B) in cells exposed to TTR-ol resulted significantly different from those detected in cells exposed to TTR-T4 or to vehicle. We observed a similar effect in cells exposed to TTR-fib; the effect arose in the same time window but its magnitude was significantly reduced as

compared to that seen in cells exposed to TTR-ol (see Table S II for statistical analysis). The reduced magnitude was consistent with the smaller cumulative calcium fractional variation induced by TTR-fib as compared to TTR-ol in HL-1 cells. This finding agrees with the Ca^{2+} release from the internal stores and the Ca^{2+} flux from the extracellular medium seen in HL-1 cells (see above). Other parameters of Ca^{2+} transient (baseline level, time to peak and decay kinetics) were not modified (Tables SIII-S V and Table II).

Finally, to assess the consequences of the altered intracellular Ca^{2+} cycling on membrane potential we performed whole-cell recordings of action potential on isolated mouse ventricular myocytes by adding TTR-ol or TTR-fib to the pipette solution. At this condition, a clear prolongation of the action potential became evident 3 min after gaining whole-cell access that persisted after 7 min, and was characterized by a marked lengthening of the plateau phase (Fig. 7C). The observed effect on membrane potential is in line with the increase of cytosolic Ca^{2+} reported above and confirms the interference of oligomeric and fibrillar TTR with the electrophysiological properties of the investigated CMs.

Discussion

Cardiomyopathy is the most frequent and severe complication of TTR amyloidosis both in the familial (FAC) and in the senile (SSA) forms. The lack of effective pharmacological treatments for these conditions is, at least in part, the consequence of the reduced information on the key factors underlying TTR misfolding and aggregation in tissue as well as on the molecular features of the biochemical, functional and viability impairment of cardiac cells exposed to aggregated TTR. Presently, the cytotoxicity of amyloid aggregates, particularly those arising early in the aggregation path, is considered amongst the main factors responsible for cell functional and viability impairment (15, 49), even though cell sufferance can also result from the physical barrier to nutrient exchange represented by the fibrillar deposits (52).

In this study, we investigated how different wtTTR forms, including the non-amyloidogenic, stabilized T4-bound derivative and amyloidogenic TTR including prefibrillar assemblies (TTR-ol) and mature fibrils (TTR-fib), affect the viability and some biochemical parameters in exposed CMs. These data were added to those provided by electrophysiological experiments on the early functional alterations occurring in exposed cardiac cells in terms of Ca^{2+} transients and membrane potential. In our experimental model, the TTR-fib sample contained a heterogeneous mixture of prefibrillar and fibrillar components as showed by DOT immunostaining. This sample makes sense if one considers that cardiac cells are exposed to tissue deposits where TTR is aggregated in the fibrillar form, and that oligomeric and/or protofibrils entities can also be present either as intermediates in the aggregation path (12, 13) and/or following leakage from the fibrillar deposits, as reported for other aggregated proteins (53).

We initially characterized the aggregated forms used in this study by investigating in depth by FT-IR, CR, DLS and AFM the path of TTR aggregation at pH 4.4 or 7.4 as well as aggregate morphology. The aggregation of wtTTR, but not TTR-T4, at pH 4.4 displayed the well-known path, where early oligomers are progressively replaced by mature fibrils as far as aggregation proceeds. The protein did not aggregate at pH 7.4, even for long incubation times, as previously reported (15). Then, we investigated whether, where, and how the different TTR aggregates were able to interact with the sarcolemma of the exposed cells. Prefibrillar TTR assemblies and TTR fibrils interacted with the plasma membrane of CMs and such interaction required the negatively charged sialic acid moiety of the ganglioside GM1, a key lipid raft component, even though we cannot exclude some contribution coming from the sialic acid residues bound to membrane glycoproteins. In this regard, there are some clear qualitative commonalities with data obtained in other cell types, namely neurons, and with aggregates grown from different peptides/proteins: amyloid aggregation and aggregate recruitment are favored by GM1-rich sites of the cell membrane (50, 54-55) and, more generally, by negatively charged surfaces (56-60). This observation can also provide clues to speculate that an increase in GM1 content in aged CMs could favor TTR aggregation in SSA, as previously shown in amyloid-positive synaptosomes from Alzheimer's brains (56); however, as far as we know, data on GM1 content in aged CMs are not available. In our experimental condition, the colocalization analysis showed that fibrillar component promoted a higher GM1 recruitment than the prefibrillar component, suggesting a higher activity of the fibrils on cell membrane uptake by raft components and subsequent membrane damage. Accordingly, recent paper suggest that the amyloid toxicity is mediated by cellular factors that interact with protofibrils and fibrils inducing further protein fibrillization on the cell surface that, in turn, triggers downstream a cascade of intracellular events compromising cell survival (30). The importance of lipid rafts in TTR recruitment by the plasma membrane of the exposed cells is indirectly confirmed by a recent study reporting that a reduction of membrane cholesterol, a key component of lipid rafts, significantly impaired the interaction and subsequent internalization of two TTR variants (I122V and T119M) with the plasma membrane of exposed CMs (the AC16 line) (32). Even though the authors exposed cells to soluble, non-aggregated proteins, they are aware of the problem to assess which precise TTR species are involved in cell damage. They speculated about the possibility that the samples of their soluble amyloidogenic V121I TTR contained tiny amounts of oligomer populations that would interact preferentially with the exposed cells. If so, their condition would resemble our well-controlled approach.

TTR-ol and TTR-fib displayed significant cytotoxicity, but they did not result in cell death at our conditions, in accordance with their ability to interact with the plasma membrane, to be internalized (in the case of TTR-ol), to induce

intracellular ROS production, to alter intracellular Ca^{2+} homeostasis and mitochondrial membrane potential. The latter effects were, at least in part, the consequence of membrane permeabilization to calcium; in fact, increase in intracellular Ca^{2+} concentration and mitochondrial membrane potential perturbation were not seen in cells cultured in Ca^{2+} -free medium or exposed to the stabilized TTR-T4, unable to bind to the plasma membrane. The hampered Ca^{2+} rise in cells treated with inhibitors of the ryanodine and IP₃-receptors before exposure to aggregated TTR suggests that such an increase depends, at least in part, on the release from SR stores through either receptor. Similar findings were previously reported in mouse neuronal cells exposed to TTR oligomers (16), suggesting the existence of shared basic alterations induced by TTR aggregates in different cell types and a possible pathophysiologic basis for multi-organ failure in TTR amyloidosis. In our model, it is possible that the increased Ca^{2+} initially came from the extracellular medium and only subsequently from the intracellular stores by Ca^{2+} -induced calcium release (CICR), an important mechanism of Ca^{2+} handling in cardiac cells (61). We cannot exclude that the effects at the mitochondrial and SR membrane result, at least in part, from the interaction with the internalized oligomers; however, the same effects were also found in cells exposed to TTR-fib, where intracellular oligomers were absent. More likely, the mitochondrial membrane depolarization could result from the increased levels of free intracellular Ca^{2+} , as reported in other cases (62). In the case of TTR-fib, which does not penetrate inside the cells, a different mechanism, either alternative or additive, can be hypothesized; this could involve fibril interaction with death receptors or Ca^{2+} channels, as previously shown for amyloid fibrils grown from Sup35NM (27) or ataxin-3 (50). This scenario supports the idea that, in TTR amyloidosis, same disturbance of cell/tissue function by the deposits of fibrillar material results not only from mechanical alteration of proper oxygen and nutrients exchange, but also from more subtle biochemical and physiological modifications resulting from the interaction of deposited fibrils and/or leaked oligomers with surrounding cells. Several lines of evidence implicate amyloid oligomers as the main cytotoxic species, even though not all oligomers are indeed cytotoxic (63, 64); however amyloid fibrils cytotoxicity is not surprising since it has been repeatedly reported (19-23). In addition, given the high complexity of the fibrillation process and considering the overall dynamics in the assembly and disassembly of toxic amyloid species, the possibility that toxicity is displayed by different conformers should not be disregarded; moreover, it has also been suggested that the ongoing aggregation process rather than a clearly defined aggregate is responsible for amyloid toxicity (30, 31).

Our findings on Ca^{2+} dyshomeostasis in exposed CMs reveal the occurrence of early effects, which likely precede or parallel those affecting cell viability and mitochondrial physiology. In cell culture all these effects develop within minutes from cell exposure to the aggregates, as shown by the temporal dynamics of Ca^{2+} levels and action potential recordings. A similar time course of cytoplasmic Ca^{2+} increase has been reported in peripheral sensory neurons exposed to TTR aggregates, where the effects were mediated by a gain of function of different ion channels, namely voltage-gated calcium and sodium channels and transient receptor potential M8 channels (14). Assessing whether in our setting the enhanced intracellular Ca^{2+} results from similar modifications deserves further investigation. In line with this observation, our findings on perturbation of intracellular Ca^{2+} homeostasis do not exclude or may also concur with multiple modifications of different ion channels and/or pumps, which altogether contribute to define the functional profile of CMs. However, a comprehensive exploration of each specific ionic modification potentially induced by TTR variants requires dedicated investigations beyond the aims of the present study. Interestingly, in sensory neurons one of the mechanisms supposed to explain Ca^{2+} rise is TTR interaction with cholesterol-rich regions of membranes able to promote ion channel opening. Such a hypothesis is in line with previous findings (32, 57, 65) and with our present data showing a preferential interaction of TTR aggregates with GM1-rich sites, presumably in lipid rafts. Of note, GM1-rich sites have been shown to co-localize with, and to modulate, ion channel function in the plasma membrane of different cell types (66-71) and with the sodium calcium exchanger in the nuclear envelope of cardiomyocytes (72).

Besides cell viability and mitochondrial efficiency, the increase in Ca^{2+} transient amplitude observed in electrically-stimulated ventricular CM exposed to TTR aggregates are in agreement with their ability to mobilize cytosolic Ca^{2+} . Indeed, in CMs a complex network involving plasmalemma, SR receptors (namely ryanodine but also IP₃ receptors) and mitochondria is responsible to finely tune cytosolic Ca^{2+} (73-75). In this interplay, the mitochondria serve as an efficient dynamic buffer of the Ca^{2+} released during contraction. The interplay, inside cells, between oxidative metabolism, calcium levels, ATP and ROS production and protein aggregation has been previously outlined (75). It is possible that ionic mechanisms accomplishing this function at the mitochondrial membrane are impaired by TTR aggregate-induced membrane depolarization, thus contributing to cytoplasmic Ca^{2+} rise. Whatever the source of Ca^{2+} accumulation inside the CMs, this effect is expected invariably to have relevant consequences in terms of generation and propagation of electrical impulses. Indeed, an increase in intracellular calcium concentration is a common feature of several acquired or congenital cardiomyopathies: for sake of comparison, a 40% increase in diastolic Ca^{2+} level was measured in cardiomyocytes from patients with hypertrophic cardiomyopathy, compared to control cells (76). Such an increase is sufficient to predispose cardiomyocytes to contractile dysfunction and occurrence of arrhythmogenic mechanisms (75). Accordingly, action potential recordings in mouse ventricular myocytes exposed to TTR aggregates show a remarkable prolongation of repolarization with a pronounced increase of the plateau level. Both events are suggestive of increased cytosolic Ca^{2+} levels, in agreement with our findings on TTR aggregate-induced Ca^{2+} accumulation and with previous studies in isolated CMs (77).

Conclusion

Taken together, the alterations of the mechanisms controlling intracellular Ca²⁺ homeostasis and the prolongation of the duration of the action potential may alter the functional properties of CMs favoring the development of cellular arrhythmias. These effects, besides further supporting the idea that specific cellular abnormalities are induced by TTR aggregates in the heart parenchyma, may also represent a basis for the occurrence of rhythm disturbances and conduction alterations often seen in patients with TTR amyloidosis.

Acknowledgments

This work was supported by grants from the Ente Cassa di Risparmio di Firenze, Project “lipid rafts” and from the Italian MIUR, PRIN 2009 (2009KN2FBM_002).

Author Contribution

L. S.: conception and design, collection and/or assembly of data, data analysis and interpretation, manuscript writing; **M. B.:** conception and design, collection and/or assembly of data, data analysis and interpretation, manuscript writing, financial support; **V. S.:** collection and assembly of data, calcium transient; **M. L.:** collection and assembly of data, biochemical and biophysical analysis; **A. N.:** collection and assembly of data, FTIR analysis; **D. N.:** collection and assembly of data, confocal imaging; **S. M. D.:** collection and assembly of data, FTIR analysis; **A. R.:** collection and assembly of data, AFM analysis; **A. P.:** collection and assembly of data, AFM analysis; **S. G.:** collection and assembly of data; **E. G.:** collection and assembly of data, calcium transient; **G. M.:** data analysis and interpretation, calcium transient; **V. B.:** data analysis and interpretation; **S. R.:** collection and assembly of data; **E. C.:** conception and design, data analysis and interpretation, manuscript writing, financial support; **M. S.:** conception and design, data analysis and interpretation, manuscript writing, financial support

References

1. Sambe A., Osinska H. Saffitz J.B. et al. Desmin-related cardiomyopathy in transgenic mice: a cardiac amyloidosis. *Proc. Natl. Acad. Sci. USA* 2004; 101:10132-36.
2. Willis, M.S. and Patterson, C. Proteotoxicity and cardiac dysfunction – Alzheimer’s disease of the heart? *New Engl. J. Med.* 2013; 368:455-64.
3. Rapezzi C, Merlini G, Quarta CC, Riva L, Longhi S, Leone O, Salvi F, Ciliberti P, Pastorelli, F, Biagini E, Cocco F, Cooke RM, Bacchi-Reggiani L, Sangiorgi D, Ferlini A, Cavo M, Zamagni E, Fonte ML, Palladini G, Salinaro F, Musca F, Obici L, Branzi A and Perlini, S. Systemic cardiac amyloidoses: disease profiles and clinical courses of the 3 main types. *Circulation*. 2009; 120:1203-12.
4. Snyder EL, Nichols WC, Liepnieks JJ and Benson MD. Direct evidence for the hereditary nature of senile cardiac (systemic) amyloidosis. *Am. J. Hum. Genet.* 1989; 45(suppl.):A220.
5. White JT, Kelly JW. Support for the multigenic hypothesis of amyloidosis: the binding stoichiometry of retinol-binding protein, vitamin A, and thyroid hormone influences transthyretin amyloidogenicity in vitro. *Proc Natl Acad Sci U S A.* 2001; 98(23):13019-24.
6. Ando Y, Nakamura M and Araki S. Transthyretin-related familial amyloidotic neuropathy. *Arch. Neurol.* 2005; 62:1057-62.
7. Rapezzi C, Quarta CC, Riva L, Longhi S, Gallelli I, Lorenzini M, Ciliberti P, Biagini E, Salvi F. and Branzi A. Transthyretin-related amyloidoses and the heart: a clinical overview. *Nat. Rev. Cardiol.* 2010; 7:398-408.
8. Quintas A, Saraiva MJ and Brito RM. The amyloidogenic potential of transthyretin variants correlates with their tendency to aggregate in solution. *FEBS Lett.* 1997; 418:297-300.
9. Johnson SM, Wiseman RL, Sekijima Y, Green RS, Adamski-Werner SL and Kelly JW. Native state kinetic stabilization as a strategy to ameliorate protein misfolding diseases: a focus in the transthyretin amyloidoses. *Acc Chem Res.* 2005; 38:911-21.

10. Hou X, Aguilar M-I and Small DH. Transthyretin and familial amyloidotic polyneuropathy. Recent progress in understanding the molecular mechanism of neurodegeneration. *FEBS J.* 2007; 274:1637-50.
11. Miroy GJ, Lai Z, Lashuel HA, Peterson C, Strang C and Kelly JW. Inhibiting transthyretin amyloid fibril formation via protein stabilization. *Proc Natl Acad Sci. USA* 1996; 93:15051-56.
12. Reixach N, Deechongkit S, Jiang X, Kelly JW and Buxbaum JN. Tissue damage in the amyloidosis: transthyretin monomers and nonnative oligomers are the major cytotoxic species in tissue culture. *Proc. Natl. Acad. Sci. USA* 2004; 101:2817-22.
13. Mendes Sousa M, Cardoso I, Fernandes R, Guimaraes A and Saraiva MJ. Deposition of transthyretin in early stages of familial amyloidotic polyneuropathy. Evidence for toxicity of nonfibrillar aggregates. *Am. J. Pathol.* 2001; 159:1993-2000.
14. Gasperini RJ, Hou X, Parkington H, Coleman H, Klaver DW, Vincent AJ, Foa LC and Small DH. TRPM8 and Na_v1.8 sodium channels are required for transthyretin-induced calcium influx in growth cones of small-diameter TrkA-positive sensory neurons. *Mol. Neurodegen.* 2011; 6:19-30.
15. Hou X, Parkington HC, Coleman HA, Mechler A, Martin LL, Aguilar M-I and Small DH. Transthyretin oligomers induce calcium influx via voltage-gated calcium channels. *J. Neurochem.* 2007; 100:446-57.
16. Teixeira PF, Cerca F, Santos SD, Saraiva MJ. Endoplasmic reticulum stress associated with extracellular aggregates. Evidence from transthyretin deposition in familial amyloid polyneuropathy. *J Biol Chem.* 2006; 281:21998-22003.
17. Misumi Y, Ueda M, Obayashi K, Jono H, Su Y, Yamashita T, Ohshima T, Ando Y and Uchino M. Relationship between amyloid deposition and intracellular structural changes in familial amyloidotic polyneuropathy. *Human. Pathol.* 2012; 43:96-104.
18. Mendes Sousa M, Fernandes R, Almeida Palha JH, Taboada A, Viera P and Saraiva MJ. Evidence for early cytotoxic aggregates in transgenic mice for human transthyretin Leu55Pro. *Am J Pathol.* 2002; 161:1935-48.
19. Gharibyan AL, Zamotin V, Yanamandra K, Moskaleva OS, Margulis BA, Kostanyan IA, Morozova-Roche LA. Lysozyme amyloid oligomers and fibrils induce cellular death via different apoptotic/necrotic pathways. *J Mol Biol.* 2007; 365: 1337-1349.
20. Mossuto MF, Dhulesia A, Devlin G, Frare E, Janet R, Kumita JR, Polverino de Laureto P, Dumoulin M, Fontana A, Dobson CM, Salvatella X. The Non-Core Regions of Human Lysozyme Amyloid Fibrils Influence Cytotoxicity. *J. Mol. Biol.* 2010; 492:783-96.
21. Pieri L, Madiona K, Bousset L, Melki R Fibrillar α -synuclein and huntingtin exon 1 assemblies are toxic to the cells. *Biophys. J.* 2012; 102:2894-2905.
22. Mocanu MM, Ganea C, Siposova K, Filippi A, Demjen E, Marek J, Bednarikova Z, Antosova A, Baran I, Gazova Z Polymorphism of hen egg white lysozyme amyloid fibrils influences the cytotoxicity in LLC-PK1 epithelial kidney cells. *Int J Biol Macromol.* 2014; 65: 176-87.
23. Harte NP, Klyubin I, McCarthy EK, Min S, Garrahy SA, Xie Y, Davey GP, Boland JJ, Rowan MJ, Mok KH. Amyloid Oligomers and Mature Fibrils Prepared from an Innocuous Protein Cause Diverging Cellular Death Mechanisms. *J Biol Chem.* 2015;290(47):28343-52.
24. Fukunaga S, Ueno H, Yamaguchi T, Yano Y, Hoshino M, Matsuzaki K. GM1 cluster mediates formation of toxic A β fibrils by providing hydrophobic environments. *Biochemistry.* 2012; 51(41): 8125-31.
25. Lee YJ, Savtchenko R, Ostapchenko VG, Makarava N, Baskakov IV. Molecular structure of amyloid fibrils controls the relationship between fibrillar size and toxicity. *PLoS One.* 2011; 6(5): e20244. doi: 10.1371/journal.pone.0020244.

26. Pieri L, Bucciantini M, Nosi D, Formigli L, Savistchenko J, Melki R, Stefani M. The yeast prion Ure2p native-like assemblies are toxic to mammalian cells regardless of their aggregation state. *J Biol Chem.* 2006; 281(22):15337-44.
27. Bucciantini M, Nosi D, Forzan M, Russo E, Calamai M, Pieri L, Formigli L, Quercioli F, Soria S, Pavone F, Savistchenko J, Melki R, Stefani M. Toxic effects of amyloid fibrils on cell membranes: the importance of ganglioside GM1. *FASEB J.* 2012; 26(2):818-31.
28. Leri M, Nosi D, Natalello A, Porcari R, Ramazzotti M, Chiti F, Bellotti V, Doglia SM, Stefani M, Bucciantini M. The polyphenol Oleuropein aglycone hinders the growth of toxic transthyretin amyloid assemblies. *J Nutr Biochem.* 2016;30:153-66.
29. Leri M, Bemporad F, Oropesa-Nuñez R, Canale C, Calamai M, Nosi D, Ramazzotti M, Giorgetti S, Pavone FS, Bellotti V, Stefani M, Bucciantini M. Molecular insights into cell toxicity of a novel familial amyloidogenic variant of β 2-microglobulin. *J Cell Mol Med.* 2016; 20(8):1443-56.
30. Jan A, Adolfsson O, Allaman I, Buccarello AL, Magistretti PJ, Pfeifer A, Muhs A, Lashuel HA. Abeta42 neurotoxicity is mediated by ongoing nucleated polymerization process rather than by discrete Abeta42 species. *J Biol Chem.* 2011;286(10):8585-96.
31. E. Hubin · N. A. J. van Nuland · K. Broersen · K. Pauwels. Transient dynamics of A β contribute to toxicity in Alzheimer's disease *Cell. Mol. Life Sci.* (2014) 71:3507–3521
32. Manral P and Reixach N. Amyloidogenic and non-amyloidogenic transthyretin variants interact differently with human cardiomyocytes: insights into early events of non-fibrillar tissue damage. *Biosci Rep Epub.* 2015 Jan 14;35(1). pii: e00172. doi: 10.1042/BSR20140155
33. Natalello A, Mattoo RU, Priya S, Sharma SK, Goloubinoff P, Doglia SM. Biophysical characterization of two different stable misfolded monomeric polypeptides that are chaperone-amenable substrates. *J Mol Biol.* 2013; 425(7):1158-71.
34. Natalello A, Ami D, Collini M, D'Alfonso L, Chirico G, Tonon G, Scaramuzza S, Schrepfer R, Doglia SM. Biophysical characterization of Met-G-CSF: effects of different site-specific mono-pegylations on protein stability and aggregation. *PLoS One.* 2012; 7(8):e42511.
35. Claycomb WC, Lanson NA Jr, Stallworth BS, Egeland DB, Delcarpio JB, Bahinski A and Izzo NJ Jr. HL-1 cells: a cardiac muscle cell line that contracts and retains phenotypic characteristics of the adult cardiomyocyte. *Proc Natl Acad Sci USA.* 1998; 95:2979-84.
36. Berlinguer-Palmini R, Narducci R, Merhan K, Dilaghi A, Moroni F, Masi A, Scartabelli T, Landucci E, Sili M, Schettini A, McGovern B, Maskaant P, Degenaar P, Mannaioni G. Arrays of microLEDs and astrocytes: biological amplifiers to optogenetically modulate neuronal networks reducing light requirement. *PLoS One.* 2014 Sep 29;9(9):e108689. doi: 10.1371/journal.pone.0108689. eCollection .
37. Sartiani L, Cerbai E, Lonardo G, DePaoli P, Tattoli M, Cagiano R, Carratù MR, Cuomo V, Mugelli A. Prenatal exposure to carbon monoxide affects postnatal cellular electrophysiological maturation of the rat heart: a potential substrate for arrhythmogenesis in infancy. *Circulation.* 2004; 109(3):419-23.
38. Wang SS, Rymer DL and Good TA. Reduction in cholesterol and sialic acid content protect cells from the toxic effects of beta-amyloid peptides. *J Biol Chem.* 2001; 42027-34.
39. Ami D, Ricagno S, Bolognesi M, Bellotti V, Doglia SM and Natalello A. Structure, stability, and aggregation of β -2 microglobulin mutants: insights from a Fourier transform infrared study in solution and in the crystalline state. *Biophys. J.* 2012; 102:1676-84.

40. Cordeiro Y, Kraineva J, Suarez MC, Tempesta AG, Kelly JW, Silva JL, Winter R and Foguel D. Fourier transform infrared spectroscopy provides a fingerprint for the tetramer and for the aggregates of transthyretin. *Biophys J.* 2006; 91:957-67.
41. Zandomenighi G, Krebs MRH, McCammon MG and Fandrich M. FTIR reveals structural differences between native beta-sheet proteins and amyloid fibrils. *Protein Sci.* 2004; 13:3314-21.
42. Pires RH, Karsai Á, Saraiva MJ, Damas AM, Kellermayer MS Distinct Annular Oligomers Captured along the Assembly and Disassembly Pathways of Transthyretin Amyloid Protofibrils. *PLoS One* 2012; 7: e44992. doi: 10.1371/journal.pone.0044992.
43. Zinchuk O. and Zinchuk V. Dynamics of cellular responses studied by quantitative colocalization analysis. *Microscopy and Analysis.* 2006; 20(5):S13-S15 (UK)
44. Hou X, Mechler A, Martin LL, Aguilar MI and Small DH. Cholesterol and anionic phospholipids increase the binding of amyloidogenic transthyretin to lipid membranes. *Biochim. Biophys. Acta* 2008; 1778:198-205.
45. Wang X, Wang W, Li L, Perry G, Lee HG, Zhu X. Oxidative stress and mitochondrial dysfunction in Alzheimer's disease. *Biochim Biophys Acta.* 2014; 1842(8):1240-1247.
46. Sartiani L, Bochet P, Cerbai E, Mugelli A, Fischmeister R. Functional expression of the hyperpolarization-activated, non-selective cation current I(f) in immortalized HL-1 cardiomyocytes. *J Physiol.* 2002; 545(Pt 1): 81-92.
47. Burt R, Graves BM, Gao M, Li C, Williams DL, Fregoso SP, Hoover DB, Li Y, Wright GL, Wondergem R. 9-Phenanthrol and flufenamic acid inhibit calcium oscillations in HL-1 mouse cardiomyocytes. *Cell Calcium.* 2013; 54(3): 193-201. Sokolov Y, Kozak JA, Kaye R, Chanturiya A, Glabe C, Hall JE Soluble amyloid oligomers increase bilayer conductance by altering dielectric structure. *J Gen Physiol.* 2006; 128:637-47.
48. Glabe CG, Kaye R. Common structure and toxic function of amyloid oligomers implies a common mechanism of pathogenesis. *Neurology.* 2006; 66(2 Suppl 1):S74-8.
49. Pellistri F, Bucciantini M, Invernizzi G, Gatta E, Penco A, Frana AM, Nosi D, Relini A, Regonesi ME, Gliozzi A, Tortora P, Robello M, Stefani M. Different ataxin-3 amyloid aggregates induce intracellular Ca²⁺deregulation by different mechanisms in cerebellar granule cells. *Biochim Biophys Acta.* 2013; 1833:3155-65.
50. Um JW, Kaufman AC, Kostylev M, Heiss JK, Stagi M, Takahashi H, Kerrisk ME, Vortmeyer A, Wisniewski T, Koleske AJ, Gunther EC, Nygaard HB, Strittmatter SM. Metabotropic glutamate receptor 5 is a coreceptor for Alzheimer β oligomer bound to cellular prion protein. *Neuron.* 2013; 79(5):887-902.
51. Campioni S, Mannini B, Zampagni M, Pensalfini A, Parrini C, Evangelisti E, Relini A, Stefani M, Dobson CM, Cecchi C, Chiti F. A causative link between the structure of aberrant protein oligomers and their toxicity. *Nat Chem Biol.* 2010; 6(2):140-7.
52. Ladiwala AR, Litt J, Kane RS, Aucoin DS, Smith SO, Ranjan S, Davis J, Van Nostrand WE, Tessier PM. Conformational differences between two amyloid β oligomers of similar size and dissimilar toxicity. *J Biol Chem.* 2012; 287(29): 24765-73.
53. Misumi Y, Ueda M, Obayashi K, Jono H, Su Y, Yamashita T, Ohshima T, Ando Y and Uchino M. Relationship between amyloid deposition and intracellular structural changes in familial amyloidotic polyneuropathy. *Hum. Pathol.* 2012; 43:96-104.
54. Stefani M. Structural features and cytotoxicity of amyloid oligomers: implications in Alzheimer's disease and other disease with amyloid deposits. *Progr. Neurobiol.* 2012; 99:226-45.
55. Xue WF, Hellewell AL, Gosal WS, Homans SW, Hewitt EW, Radford SE. Fibril fragmentation enhances amyloid cytotoxicity. *J. Biol. Chem.* 2009, 284, 34272–34282.

56. Wakabayashi M & Matsuzaki K. Ganglioside-induced amyloid formation by human islet amyloid polypeptide in lipid rafts. *FEBS Lett.* 2009; 583(17):2854-8.
57. Yamamoto N, Matsubara T, Sato T, Yanagisawa K. Age-dependent high-density clustering of GM1 ganglioside at presynaptic neuritic terminals promotes amyloid β -protein fibrillogenesis. *Biochim Biophys Acta.* 2008; 1778:2717-2726.
58. Hou X, Mechler A, Martin LL, Aguilar M-I and Small DH. Cholesterol and anionic phospholipids increase the binding of amyloidogenic transthyretin to lipid membranes. *Biochim Biophys Acta.* 2008; 1778:198-205.
59. Noborn F, O'Callaghan P, Hermansson E, Zhang X, Ancsin JB, Damas AM, Dacklin I, Presto J, Johansson J, Saraiva MJ, Lundgren E, Kisilevsky R, Westermark P, Li JP Heparan sulfate/heparin promotes transthyretin fibrillization through selective binding to a basic motif in the protein. *Proc. Natl. Acad. Sci. USA.* 2011; 108(14):5584-9.
60. Bourgault S, Solomon JP, Reixach N and Kelly JW. Sulfated Glycosaminoglycans Accelerate Transthyretin Amyloidogenesis by Quaternary Structural Conversion. *Biochemistry.* 2011; 50:1001-15.
61. Calamai M and Pavone F. Partitioning and confinement of GM1 ganglioside induced by amyloid aggregates. *FEBS Lett.* 2013; 587(9):1385-91.
62. Fabiato A. Calcium-induced release of calcium from the cardiac sarcoplasmic reticulum. *Am J Physiol.* 1983; 245: C1-C14.
63. Ferreira E, Oliveira CR, Pereira CM. The release of calcium from the endoplasmic reticulum induced by amyloid-beta and prion peptides activates the mitochondrial apoptotic pathway. *Neurobiol Dis.* 2008; 30(3):331-42.
64. Evangelisti E, Cecchi C, Cascella R, Sgromo C, Becatti M, Dobson CM, Chiti F & Stefani M Membrane lipid composition and its physicochemical properties define cell vulnerability to aberrant protein oligomers. *J. Cell Sci.* 2012; 125:2416-2427.
65. Furian AF, Rattmann YD, Oliveira MS, Royes LF, Marques MC, Santos AR, Mello CF. Nitric oxide and potassium channels mediate GM1 ganglioside-induced vasorelaxation. *Naunyn Schmiedebergs Arch Pharmacol.* 2009; 380(6):487-95.
66. Wang J, Lu ZH, Gabius HJ, Rohowsky-Kochan C, Ledeen RW, Wu G. Cross-linking of GM1 ganglioside by galectin-1 mediates regulatory T cell activity involving TRPC5 channel activation: possible role in suppressing experimental autoimmune encephalomyelitis. *J Immunol.* 2009; 182(7):4036-45.
67. Wu G1, Lu ZH, Gabius HJ, Ledeen RW, Bleich D. Ganglioside GM1 deficiency in effector T cells from NOD mice induces resistance to regulatory T-cell suppression. *Diabetes.* 2011; 60(9):2341-9.
68. Qiao GF, Cheng ZF, Huo R, Sui XH, Lu YJ, Li BY. GM1 ganglioside contributes to retain the neuronal conduction and neuronal excitability in visceral and baroreceptor afferents. *J Neurochem.* 2008; 106(4):1637-45.
69. Wu G, Lu ZH, Obukhov AG, Nowycky MC, Ledeen RW. Induction of calcium influx through TRPC5 channels by cross-linking of GM1 ganglioside associated with alpha5beta1 integrin initiates neurite outgrowth. *J Neurosci.* 2007; 27(28):7447-58.
70. Susuki K1, Baba H, Tohyama K, Kanai K, Kuwabara S, Hirata K, Furukawa K, Furukawa K, Rasband MN, Yuki N. Gangliosides contribute to stability of paranodal junctions and ion channel clusters in myelinated nerve fibers. *Glia.* 2007; 55(7):746-57.
71. Hohendanner F, McCulloch AD, Blatter LA, Michailova AP. Calcium and IP3 dynamics in cardiac myocytes: Experimental and computational perspectives and approaches. *Front Pharmacol.* 2014; 5(35):1-10.
72. Endo M. Calcium ion as a second messenger with special reference to excitation-contraction coupling. *J Pharmacol Sci.* 2006; 100(5):519-24.

73. Signore S, Sorrentino A, Ferreira-Martins J, Kannappan R, Shafaie M, Del Ben F, Isobe K, Arranto C, Wybieralska E, Webster A, Sanada F, Ogórek B, Zheng H, Liu X, Del Monte F, D'Alessandro DA, Wunimenghe O, Michler RE, Hosoda T, Goichberg P, Leri A, Kajstura J, Anversa P, Rota M. Inositol 1, 4, 5-trisphosphate receptors and human left ventricular myocytes. *Circulation*. 2013; 128(12):1286-97.
74. Yang KC, Bonini MG, Dudley SC Jr. Mitochondria and arrhythmias. *Free Radic Biol Med*. 2014; 71C:351-361.
75. Squier TC. Oxidative stress and protein aggregation during biological aging. *Exp. Gerontol.*, 2001, 36, 1539-50.
76. Coppini R, Ferrantini C, Yao L, Fan P, Del Lungo M, Stillitano F, Sartiani L, Tosi B, Suffredini S, Tesi C, Yacoub M, Olivotto I, Belardinelli L, Poggesi C, Cerbai E, Mugelli A. Late sodium current inhibition reverses electromechanical dysfunction in human hypertrophic cardiomyopathy. *Circulation*. 2013; 127, 575-584.
77. Carmeliet E. Intracellular Ca^{2+} concentration and rate adaptation of the cardiac action potential. *Cell Calcium*. 2004; 35(6):557-73.

FIGURE LEGENDS

FIGURE 1. Characterization of wt TTR by FT-IR. A: FT-IR absorption spectra of native TTR and of TTR incubated at pH 4.4 for different time lengths. B: Second derivatives of the absorption spectra reported in (A). C: Second derivatives of the absorption spectra of TTR incubated at pH 7.4 for different lengths of time. The peak positions of the main components are also given. The spectra are reported after normalization to the Amide I band area. D: Peak positions (taken from the second derivative spectra) of the main β -sheet component reported versus incubation time at pH 7.4 or pH 4.4.

FIGURE 2. Morphological characterization of TTR aggregates. A: AFM images of TTR-T4, TTR-ol and TTR-fib. Scan size 1.0 μm . B: TEM images of TTR-T4, TTR-ol and TTR-fib (scale bar 200nm). C: Dot blotting of TTR-T4, TTR-ol and TTR-fib using anti-conformational A11 and OC antibodies. Three replicates were generated and probed separately by anti-TTR, A11 and OC antibody. D: Congo Red absorption spectra of TTR-T4 (green line), TTR-ol (red line), TTR-fib (blue line). E: DLS analysis of TTR-T4, TTR-ol and TTR-fib. Volume distribution of the particle apparent hydrodynamic diameter.

FIGURE 3. Confocal analysis. Confocal images of HL-1 cells treated with wtTTR. The cells were exposed for 24 h to 10 μM (A) TTR-T4, (B) TTR-ol and (C) TTR-fib. D-E: z-projections. F-G: HL-1 cells pretreated with neuraminidases to reduce sialic acid on the cell surface and incubated for 24 h to 10 μM TTR-ol (F) and TTR-fib (G). The cells were stained with cholera toxin (green) and then were fixed, permeabilized and stained with anti-TTR antibody (red) or A11 antibody (red). H: Sialic acid quantification. HL-1 cells were treated with 11,7 mU.I. of *V. cholera* neuraminidase and 5.0 mU.I. of *A. urefaciens* neuraminidase for 1.0 h at 37 °C in serum-free medium. The sialic acid levels in the membrane fractions were analyzed enzymatically by sialic acid quantification kit. * $p < 0.05$. I: Quantitative analysis of TTR-binding on the cells. Each graph displays the mean values \pm SE and a statistical comparison between treated and TTR-T4-treated cells $n = 5$, (* $p < 0.05$, $^{\circ}p < 0.01$, $\#p < 0.001$).

FIGURE 4. Cell viability, ROS levels and mitochondria dysfunction: A-B-C: Cytotoxicity of TTR-T4, TTR-ol and TTR-fib to human HL-1 cells performed by MTT reduction assay (A), intracellular ROS production (B), JC-1 assay (C). D:

Quantification of $\Delta\psi_m$ expressed as a ratio (J-aggregates/monomer) in the different treatment groups. The values shown are normalized against the buffer control (n=3, mean \pm s.d.). The statistic was analysed by unpaired Student's *t*-test (** p <0.01, *** p <0.001).

FIGURE 5. Effect of different TTR samples on cytoplasmic calcium levels in HL-1 cardiomyocytes. A: Time course of cytosolic Ca^{2+} signal detected in HL-1 CMs exposed to 10 μ M TTR-ol or TTR-fib (monomer concentration) for 20 min before SR depletion with 10 mM caffeine. B: Mean fractional variation (\pm standard error of the mean) relative to vehicle of cumulative cytosolic Ca^{2+} calculated after 20 min exposure to different experimental conditions. Abbreviations: Veh, vehicle; TTR-ol, oligomeric transthyretin; TTR-fib, fibrillar transthyretin; TTR-T4, native TTR complex with thyroid hormone; TTR-ol 0 Ca, oligomeric TTR in Ca^{2+} -free medium; TTR-fib 0 Ca, fibrillar TTR in Ca^{2+} -free medium; TTR-ol Rya, oligomeric TTR plus ryanodine; TTR-ol 2APB, oligomeric TTR plus 2APB; TTR-fib Rya, fibrillar TTR plus ryanodine; TTR-fib 2APB, fibrillar TTR plus 2APB. Statistical analysis (ANOVA followed by Tukey's multiple comparisons test) is reported in Table S I.

FIGURE 6. Effect of different TTR samples on cytoplasmic calcium levels in automatic HL-1 cardiomyocytes. A: Time course of cytosolic Ca^{2+} signal detected in automatic HL-1 CMs exposed to Vehicle (A), 10 μ M TTR (B), TTR-ol (C), TTR-ol in Ca^{2+} -free medium (D), TTR-ol plus ryanodine (E), TTR-ol plus 2APB (F), TTR-fib (G), TTR-fib in Ca^{2+} -free medium (H), TTR-fib plus ryanodine (I), TTR-fib plus 2APB (J), TTR-T4 (K), TTR-T4 in Ca^{2+} -free medium (L), TTR-T4 plus ryanodine (M), TTR-T4 plus 2APB (N), for 20 min before SR depletion with 10 mM caffeine. Abbreviations: Veh, vehicle; TTR-ol, oligomeric transthyretin; TTR-fib, fibrillar transthyretin; TTR-T4, native TTR complex with thyroid hormone; TTR-ol 0 Ca, oligomeric TTR in Ca^{2+} -free medium; TTR-fib 0 Ca, fibrillar TTR in Ca^{2+} -free medium; TTR-T4 0 Ca, TTR-T4 in Ca^{2+} -free medium; TTR-ol Rya, oligomeric TTR plus ryanodine; TTR-ol 2APB, oligomeric TTR plus 2APB; TTR-fib Rya, fibrillar TTR plus ryanodine; TTR-fib 2APB, fibrillar TTR plus 2APB; TTR-T4 Rya, TTR-T4 plus ryanodine; TTR-T4 2APB, TTR-T4 plus 2APB.

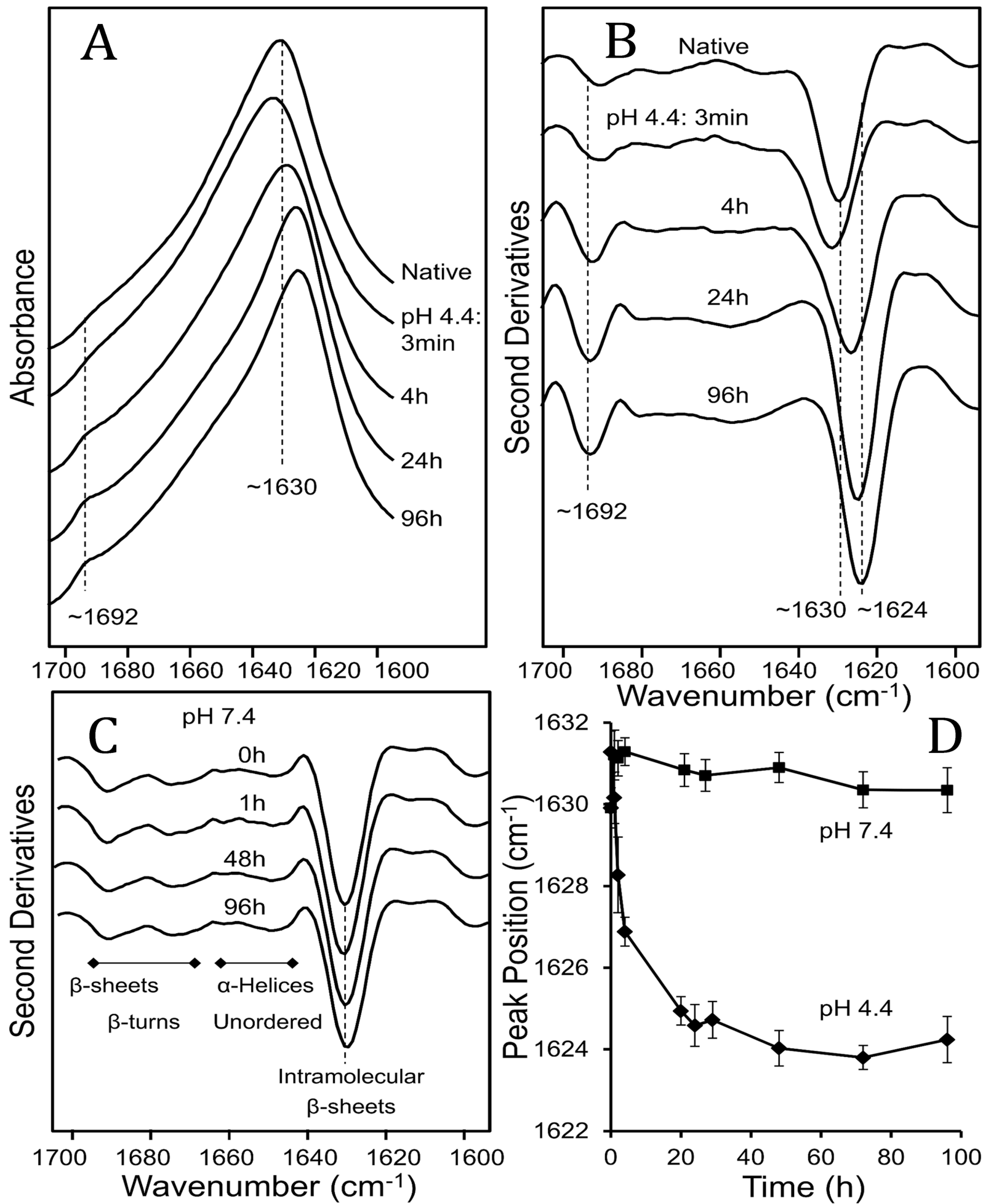
FIGURE 7. Effect of TTR variants on calcium transient and action potential of mouse ventricular myocytes. A: Representative fluorescence signals measured from ventricular CMs loaded with Fluo-4 and stimulated at 1.0 Hz pacing frequency during exposure to oligomeric TTR for 0 (a), 5 (b), 10 (c), 15 (d) and 20 (e) min. B: Time course of Ca^{2+} transient amplitude variation, expressed as mean fractional variation (\pm standard error of the mean) relative to time zero amplitude in ventricular CMs exposed to vehicle (n=18), oligomeric (n= 13), fibrillar (n=19) and wtTTR(n=14). Statistical analysis (ANOVA followed by Tukey's multiple comparisons test) is reported in Table S II. C: Representative action potential profiles measured from ventricular CMs recorded in whole-cell configuration (1.0 Hz pacing frequency) immediately after seal rupture (a and d) and after 3 or 7 min exposure to pipette solution containing 1.0 μ M TTR-ol (b and c) or TTR-fib (e and f).

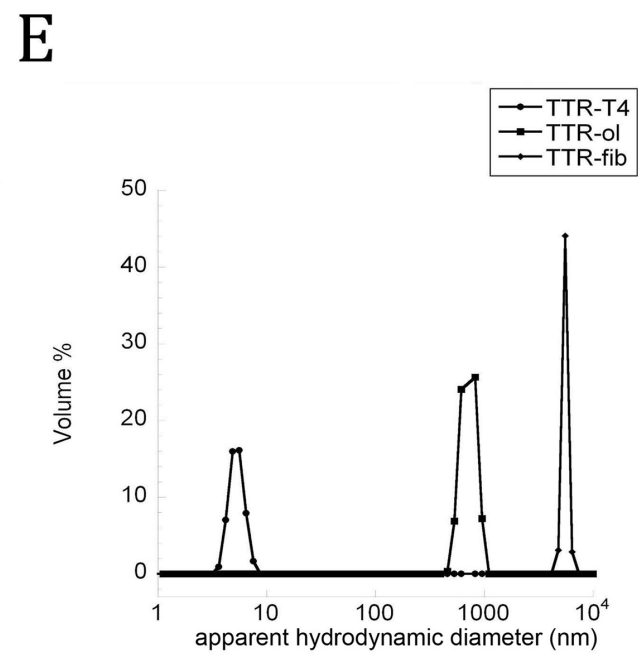
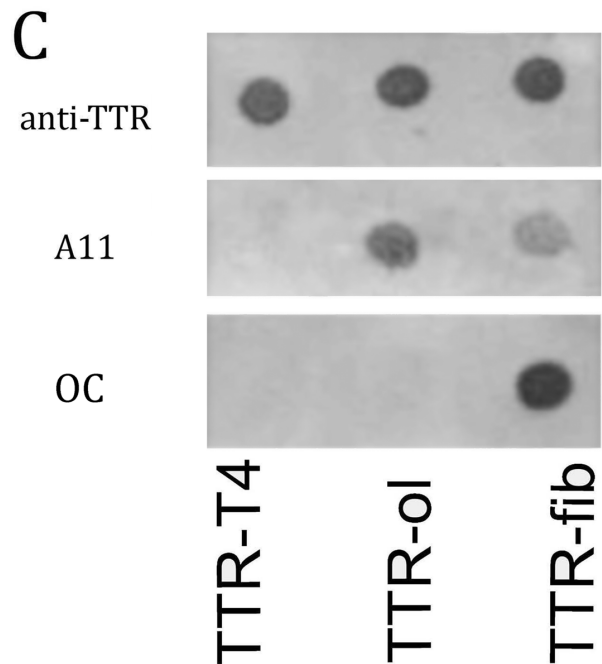
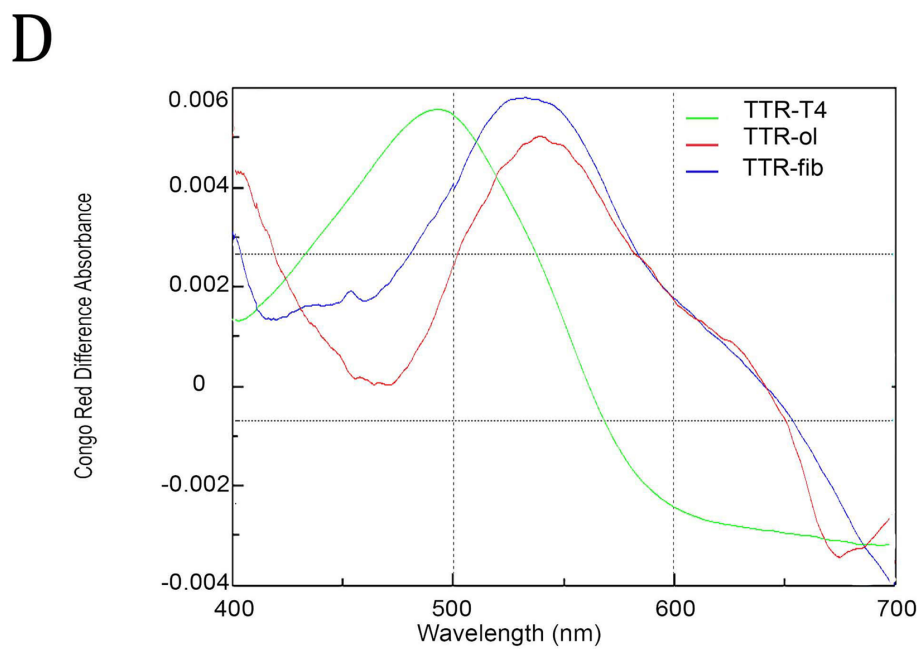
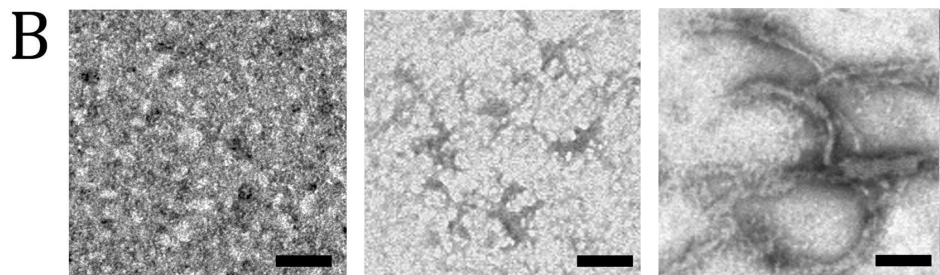
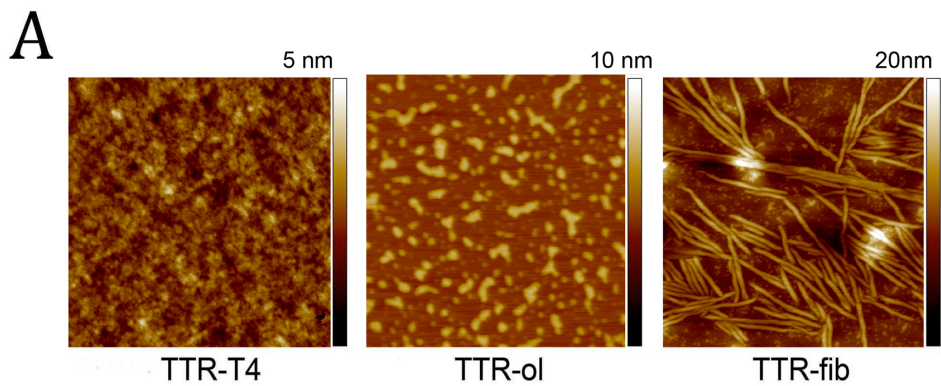
Table I: Co-localization analysis of TTR oligomers/fibrils and GM1 on the plasma membrane of HL-1 cardiomyocytes.

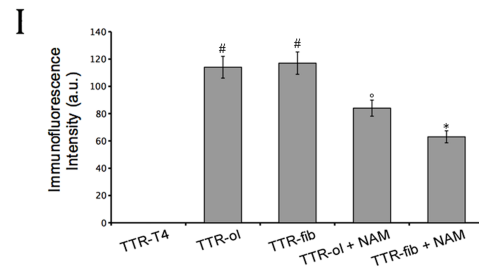
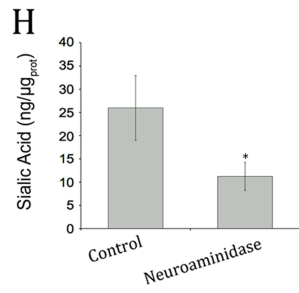
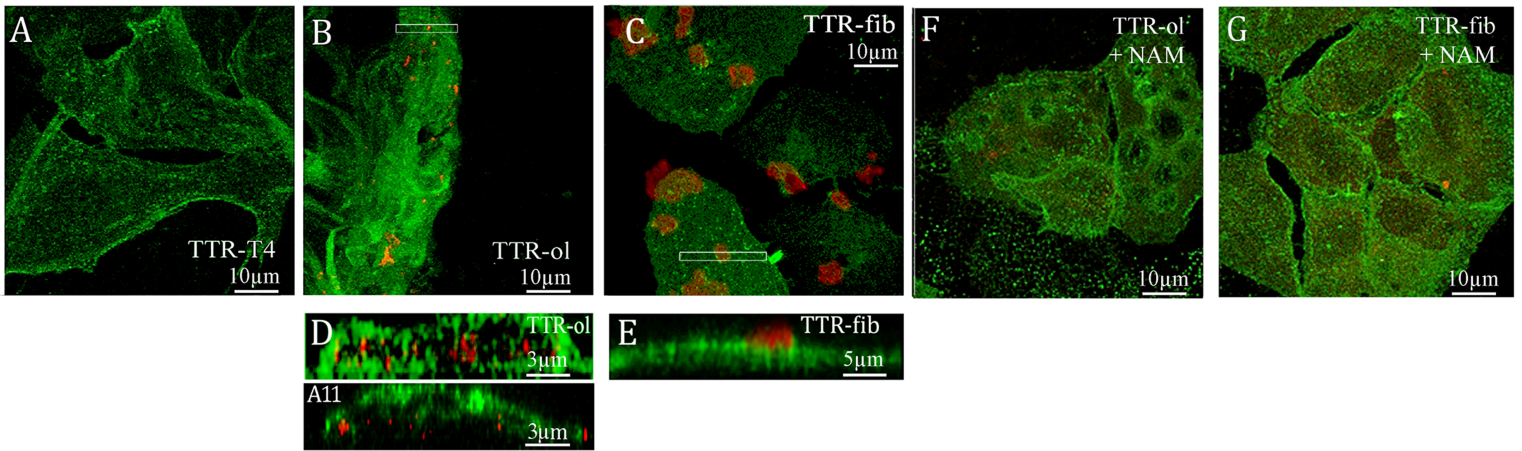
	TTR-ol	TTR-fib	TTR-ol + NAM	TTR-fib + NAM
Overlap Coefficient	0.895	0.899	0.839	0.850
k1/k2	0.855	0.448	3.070	2.56

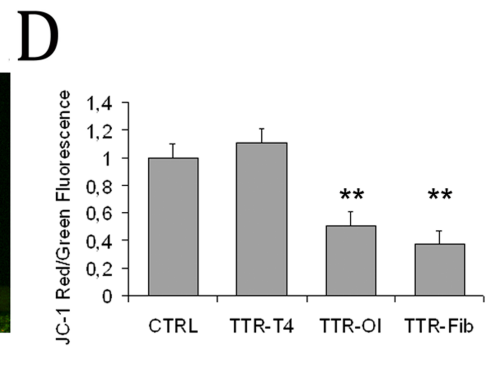
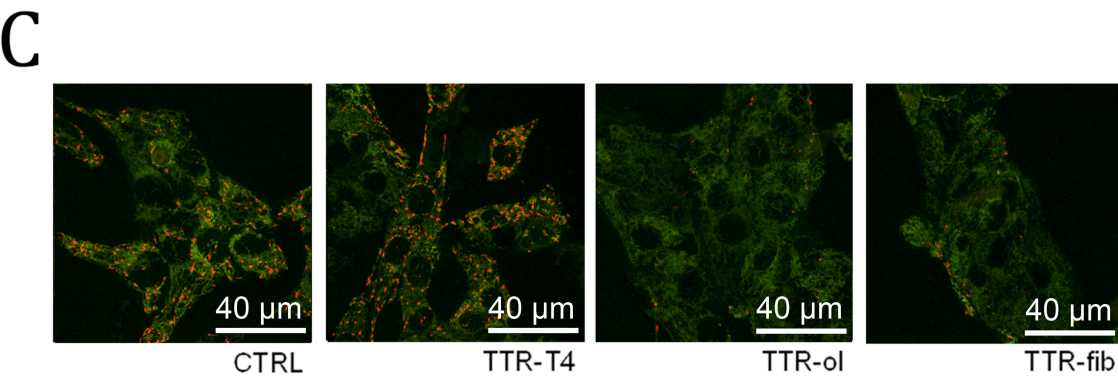
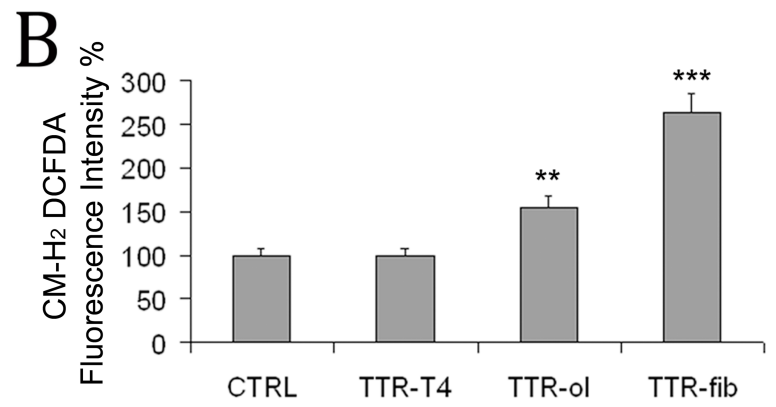
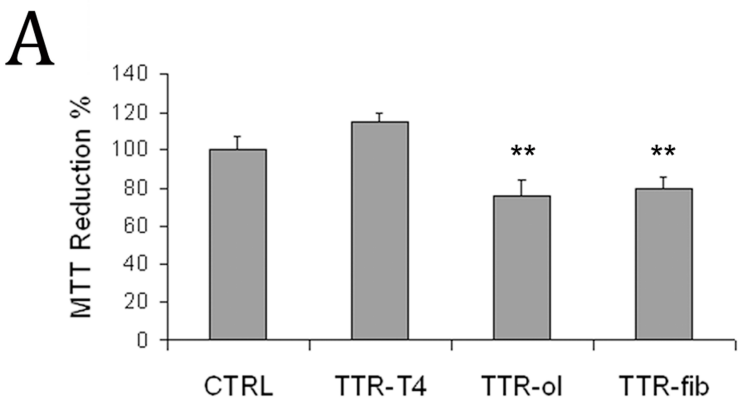
Table II: 90% decay time fractional variation of calcium transient relative to initial value in mice ventricular cardiomyocytes

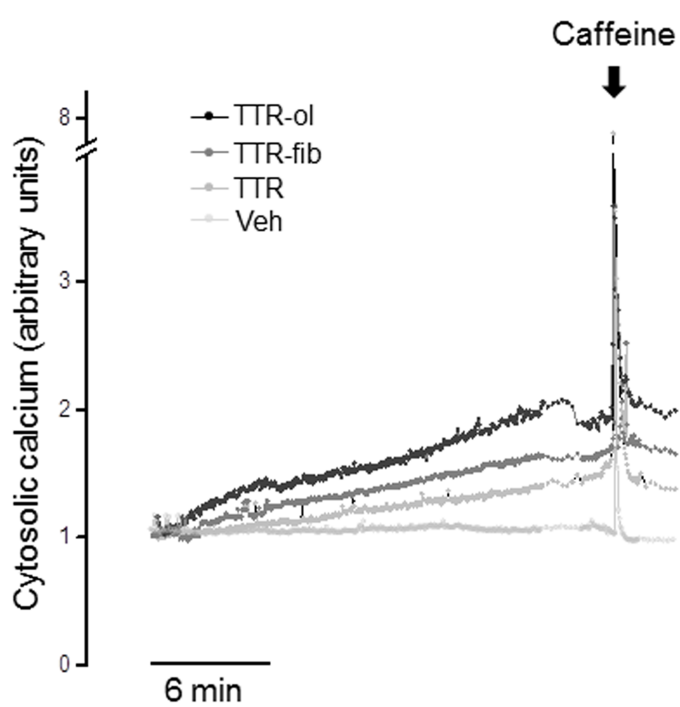
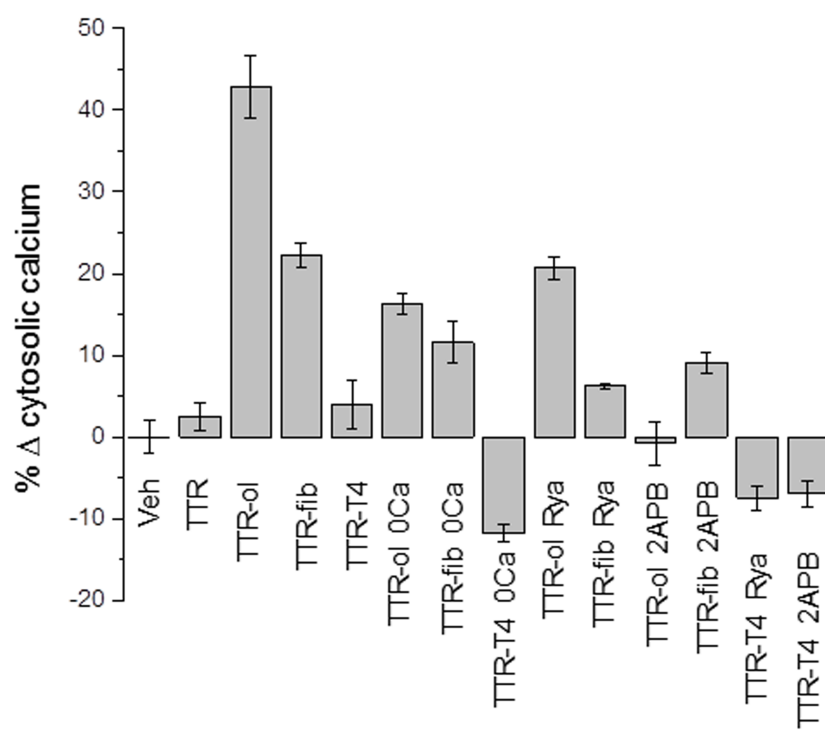
Time (min)	Vehicle (mean±s.e.m.) n=18	TTR (mean±s.e.m.) n=13	TTR-ol (mean±s.e.m.) n=14	TTR-fib (mean±s.e.m.) n=19
0	$1.1 \cdot 10^{-6} \pm 9.1 \cdot 10^{-7}$	$2.0 \cdot 10^{-7} \pm 3.1 \cdot 10^{-7}$	$8.3 \cdot 10^{-7} \pm 1.0 \cdot 10^{-6}$	$4.4 \cdot 10^{-8} \pm 1.9 \cdot 10^{-7}$
5	15.7±12.3	-7.5±8.7	14.0±12.6	10.4±3.9
10	13.9±12.0	1.3±10.3	17.0±15.3	13.2±5.1
15	30.1±18.0	16.2±10.3	40.2±23.3	25.4±10.9
20	122.4±31.4	115.7± 25.8	202.8±81.4	122.3±25.1

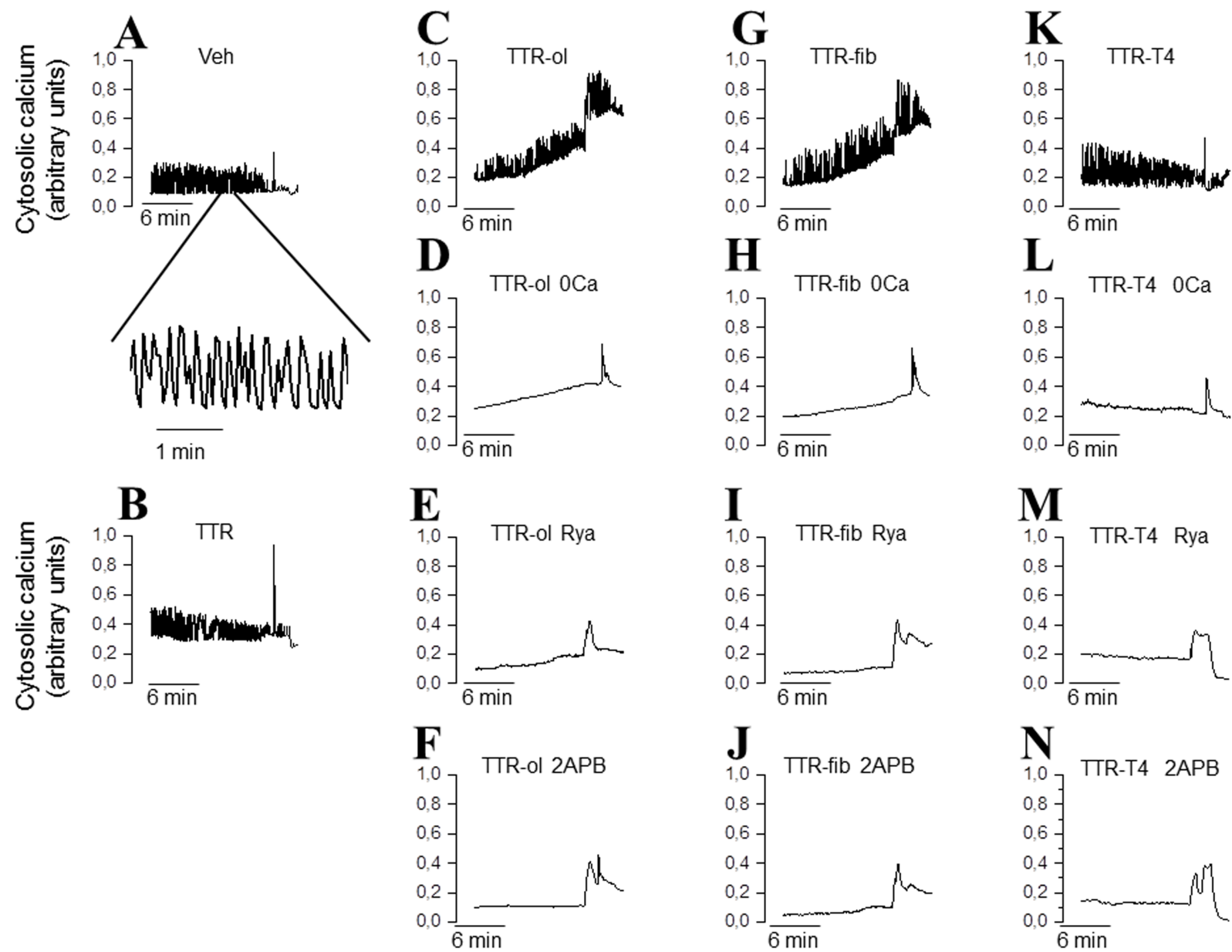


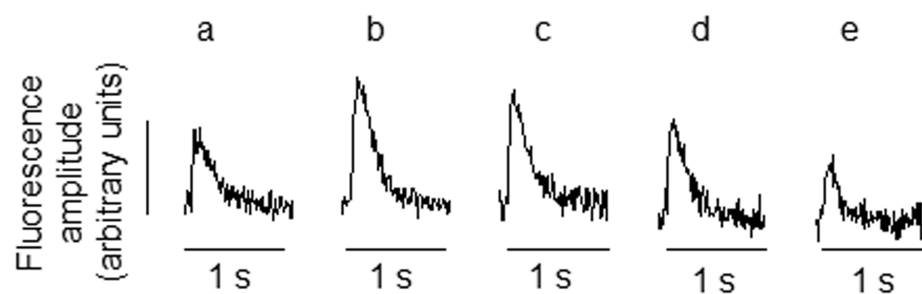
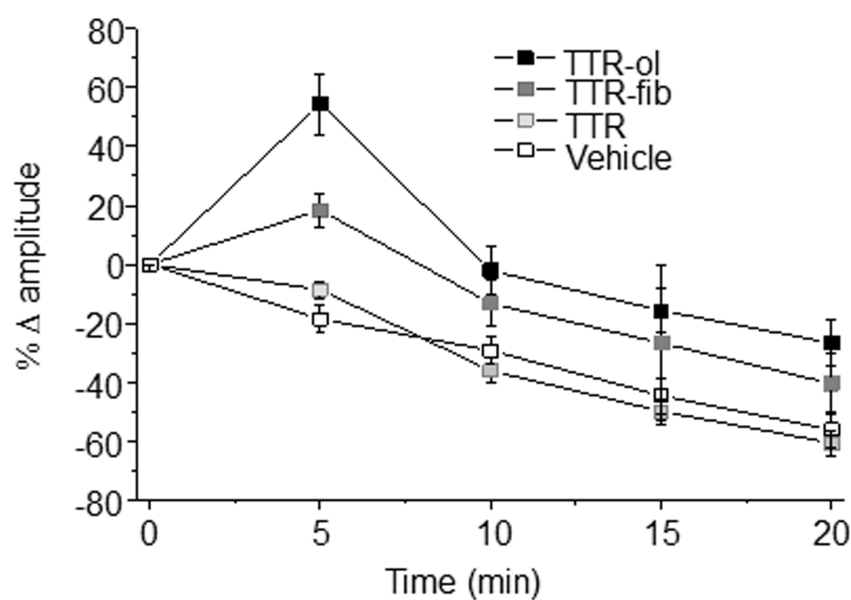
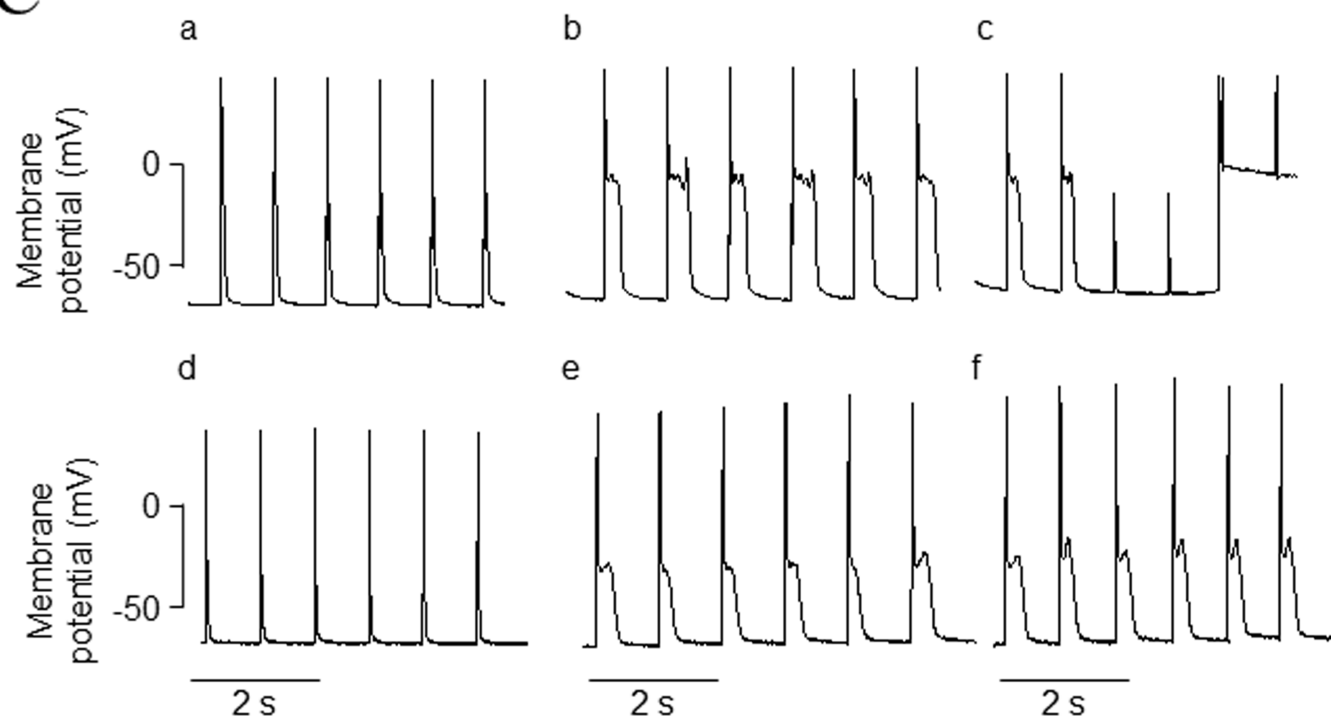






A**B**



A**B****C**

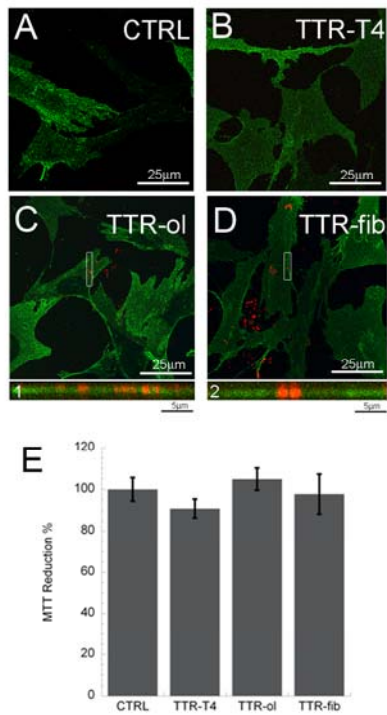


FIGURE S1. Effect of TTR variants on HDFα human cells. Confocal images of Human dermal fibroblast (HDFα) exposed for 24 h to protein buffer (A), 10 μM TTR-T4 (B), TTR-ol (C) and TTR-fib (D). The cells were stained with cholera toxin (green) and then were fixed, permeabilized and stained with anti-TTR antibody (red). 1,2: z-projection of the ROIs selected. E: Cytotoxic effect of TTR-T4, TTR-ol and TTR-fib to HDFα cells performed by the MTT reduction assay. The values shown are normalized against the buffer control (n=3, mean ±s.d.).

Table S I: Cumulative calcium fractional variation relative to vehicle in HL-1 cardiomyocytes

External solution (n)	mean±s.e.m.	P value (Tukey's multiple comparisons test)
Veh (51) vs. TTT-ol (26)	-9.1·10 ⁻⁵ ±2.0 vs. 42.9±3.8	<0.001
Veh (51) vs. TTR-fib (17)	-9.1·10 ⁻⁵ ±2.0 vs. 22.3±1.5	<0.001
Veh (51) vs. TTR-ol 0Ca (16)	-9.1·10 ⁻⁵ ±2.0 vs. 16.3±1.2	<0.01
Veh (51) vs. TTR-fib 0Ca (41)	-9.1·10 ⁻⁵ ±2.0 vs. 11.6±2.6	<0.001
Veh (51) vs. TTR-T4 0Ca (42)	-9.1·10 ⁻⁵ ±2.0 vs. -11.7±1.0	<0.001
Veh (51) vs. TTR-ol Rya (14)	-9.1·10 ⁻⁵ ±2.0 vs. 20.7±1.4	<0.001
TTR (12) vs. TTR-ol (26)	2.5±1.8 vs. 42.9±3.8	<0.001
TTR (12) vs. TTR-fib (17)	2.5±1.8 vs. 22.3±1.5	<0.05
TTR-ol (26) vs. TTR-fib (17)	42.9±3.8 vs. 22.3±1.5	<0.001
TTR-ol (26) vs. TTR-T4 (33)	42.9±3.8 vs. 4.0±3.0	<0.001
TTR-ol (26) vs. TTR-ol 0Ca (16)	42.9±3.8 vs. 16.3±1.2	<0.001
TTR-ol (26) vs. TTR-fib 0Ca (41)	42.9±3.8 vs. 11.6±2.6	<0.001
TTR-ol (26) vs. TTR-T4 0Ca (42)	42.9±3.8 vs. -11.7±1.0	<0.001
TTR-ol (26) vs. TTR-ol Rya (14)	42.9±3.8 vs. 20.7±1.4	<0.001
TTR-ol (26) vs. TTR-ol 2APB (23)	42.9±3.8 vs. 6.2±0.4	<0.001
TTR-ol (26) vs. TTR-fib Rya (20)	42.9±3.8 vs. -0.8±2.7	<0.001
TTR-ol (26) vs. TTR-fib 2APB (18)	42.9±3.8 vs. 9.1±1.2	<0.001
TTR-ol (26) vs. TTR-T4 Rya (29)	42.9±3.8 vs. -7.4±1.5	<0.001
TTR-ol (26) vs. TTR-T4+2APB (33)	42.9±3.8 vs. -6.9±1.6	<0.001
TTR-fib (17) vs. TTR-T4 (33)	22.3±1.5 vs. 4.0±3.0	<0.01
TTR-fib (17) vs. TTR-T4 0Ca (42)	22.3±1.5 vs. -11.7±1.0	<0.001
TTR-fib (17) vs. TTR-ol 2APB (23)	22.3±1.5 vs. 6.2±0.4	<0.05
TTR-fib (17) vs. TTR-fib Rya (20)	22.3±1.5 vs. -0.8±2.7	<0.001
TTR-fib (17) vs. TTR-T4 Rya (29)	22.3±1.5 vs. -7.4±1.5	<0.001
TTR-fib (17) vs. TTR-T4 2APB (33)	22.3±1.5 vs. -6.9±1.6	<0.001
TTR-T4 (33) vs. TTR-T4 0Ca (42)	4.0±3.0 vs. -11.7±1.0	<0.001
TTR-T4 (33) vs. TTR-ol Rya (14)	4.0±3.0 vs. 20.7±1.4	<0.05
TTR-ol 0Ca (16) vs. TTR-T4 0Ca (42)	16.3±1.2 vs. -11.7±1.0	<0.001
TTR-ol 0Ca (16) vs. TTR-fib Rya (20)	16.3±1.2 vs. -0.8±2.7	<0.05
TTR-ol 0Ca (16) vs. TTR-T4 Rya (29)	16.3±1.2 vs. -7.4±1.5	<0.001
TTR-ol 0Ca (16) vs. TTR-T4 2APB (33)	16.3±1.2 vs. -6.9±1.6	<0.001
TTR-fib 0Ca (41) vs. TTR-T4 0Ca (42)	11.6±2.6 vs. -11.7±1.0	<0.001
TTR-fib 0Ca (41) vs. TTR-T4 Rya (29)	11.6±2.6 vs. -7.4±1.5	<0.001
TTR-fib 0Ca (41) vs. TTR-T4 2APB (33)	11.6±2.6 vs. -6.9±1.6	<0.001
TTR-T4 0Ca (42) vs. TTR-ol Rya (14)	-11.7±1.0 vs. 20.7±1.4	<0.001
TTR-T4 0Ca (42) vs. TTR-ol 2APB (23)	-11.7±1.0 vs. 6.2±0.4	<0.001
TTR-T4 0Ca (42) vs. TTR-fib 2APB (18)	-11.7±1.0 vs. 9.1±1.2	<0.001
TTR-ol Rya (14) vs. TTR-fib Rya (20)	20.7±1.4 vs. -0.8±2.7	<0.01
TTR-ol Rya (14) vs. TTR-T4 Rya (29)	20.7±1.4 vs. -7.4±1.5	<0.001
TTR-ol Rya (14) vs. TTR-T4 2APB (33)	20.7±1.4 vs. -6.9±1.6	<0.001
TTR-ol 2APB (23) vs. TTR-T4 Rya (29)	6.2±0.4 vs. -7.4±1.5	<0.05
TTR-ol 2APB (23) vs. TTR-T4 2APB (33)	6.2±0.4 vs. -6.9±1.6	<0.05
TTR-fib 2APB (18) vs. TTR-T4 Rya (29)	9.1±1.2 vs. -7.4±1.5	<0.01
TTR-ol 2APB (23) vs. TTR-T4 2APB (33)	6.2±0.4 vs. -6.9±1.6	<0.01

Table S II: Amplitude fractional variation of calcium transient relative to initial value in mice ventricular cardiomyocytes

External solution (n)/time (minute)	mean±s.e.m.	P value (Tukey's multiple comparisons test)
Veh (18)/0 vs. Veh (18)/5	-0.012±0.012 vs. -8.59±2.90	ns
Veh (18)/0 vs. Veh (18)/10	-0.012±0.012 vs. -36.09±4.27	<0.001
Veh (18)/0 vs. Veh (18)/15	-0.012±0.012 vs. -49.85±4.29	<0.001
Veh(18)/0 vs. Veh (18)/20	-0.012±0.012 vs. -60.62±4.19	<0.001
Veh (18)/0 vs. TTR-ol (14)/0	-0.012±0.012 vs. $-1.33 \cdot 10^{-5} \pm 1.66 \cdot 10^{-5}$	ns
Veh (18)/0 vs. TTR (13)/0	-0.012±0.012 vs. $2.059 \cdot 10^{-5} \pm 4.038 \cdot 10^{-5}$	ns
Veh (18)/0 vs. TTR-fib (19)/0	-0.012±0.012 vs. $6.25 \cdot 10^{-4} \pm 4.93 \cdot 10^{-4}$	ns
Veh (18)/5 vs. Veh (18)/10	-8.59±2.90 vs. -36.09±4.27	<0.05
Veh (18)/5 vs. Veh (18)/15	-8.59±2.90 vs. -49.85±4.29	<0.001
Veh (18)/5 vs. Veh (18)/20	-8.59±2.90 vs. -60.62±4.19	<0.001
Veh (18)/5 vs. TTR-fib (19)/5	-8.59±2.90 vs. 18.39±5.64	<0.05
Veh (18)/10 vs. Veh (18)/15	-36.09±4.27 vs. -49.85±4.29	ns
Veh (18)/10 vs. Veh (18)/20	-36.09±4.27 vs. -60.62±4.19	ns
Veh (18)/10 vs. TTR-ol (14)/10	-36.09±4.27 vs. -2.01±7.90	<0.001
Veh (18)/10 vs. TTR-fib (19)/10	-36.09±4.27 vs. -9.82±7.87	<0.05
Veh (18)/15 vs. Veh (18)/20	-49.85±4.29 vs. -60.62±4.19	ns
Veh (18)/15 vs. TTR-ol (14)/15	-49.85±4.29 vs. -15.68±7.57	<0.001
Veh (18)/15 vs. TTR (13)/15	-49.85±4.29 vs. -44.51±6.13	ns
Veh (18)/15 vs. TTR-fib (19)/15	-49.85±4.29 vs. -30.47±26.14	ns
Veh (18)/20 vs. TTR-ol (14)/20	-60.62±4.19 vs. -26.72±7.88	<0.001
Veh (18)/20 vs. TTR (13)/20	-60.62±4.19 vs. -56.19±5.74	ns
Veh (18)/20 vs. TTR-fib (19)/20	-60.62±4.19 vs. -46.49±7.83	ns
TTR-ol (14)/0 vs. TTR (13)/0	$-1.33 \cdot 10^{-5} \pm 1.66 \cdot 10^{-5}$ vs. $2.06 \cdot 10^{-5} \pm 4.04 \cdot 10^{-5}$	ns
TTR-ol (14)/0 vs. TTR-fib (19)/0	$-1.33 \cdot 10^{-5} \pm 1.66 \cdot 10^{-5}$ vs. $6.25 \cdot 10^{-4} \pm 4.93 \cdot 10^{-4}$	ns
TTR-ol (14)/5 vs. TTR (13)/5	54.47±10.30 vs. -18.50±4.85	<0.001
TTR-ol (14)/5 vs. TTR-fib (19)/5	54.47±10.30 vs. 18.39±5.64	<0.001
TTR-ol (14)/10 vs. TTR (13)/10	-2.01±7.90 vs. 29.26±4.48	ns
TTR-ol (14)/10 vs. TTR-fib (19)/10	-2.01±7.90 vs. -9.82±7.87	ns
TTR-ol (14)/15 vs. TTR (13)/15	-15.68±7.57 vs. -44.51±6.13	ns
TTR-ol (14)/15 vs. TTR-fib (19)/15	-15.68±7.57 vs. -30.47±26.14	ns
TTR-ol (14)/20 vs. TTR (13)/20	-26.72±7.88 vs. -56.19±5.74	ns
TTR-ol (14)/20 vs. TTR-fib (19)/20	-26.72±7.88 vs. -46.49±7.83	ns
TTR (13)/0 vs. TTR-fib (19)/0	$2.06 \cdot 10^{-5} \pm 4.04 \cdot 10^{-5}$ vs. $6.25 \cdot 10^{-4} \pm 4.93 \cdot 10^{-4}$	ns
TTR (13)/5 vs. TTR-fib (19)/5	-18.50±4.85 vs. 18.39±5.64	<0.001
TTR (13)/10 vs. TTR-fib (19)/10	29.26±4.48 vs. -9.82±7.87	ns
TTR (13)/15 vs. TTR-fib (19)/15	-44.51±6.13 vs. -30.47±26.14	ns
TTR (13)/20 vs. TTR-fib (19)/20	-56.19±5.74 vs. -46.49±7.83	ns

Table S III: Baseline fractional variation of calcium transient relative to initial value in mice ventricular cardiomyocytes

Time (min)	Vehicle (mean±s.e.m.) n=18	TTR (mean±s.e.m.) n=13	TTR-ol (mean±s.e.m.) n=14	TTR-fib (mean±s.e.m.) n=19
------------	----------------------------	------------------------	---------------------------	----------------------------

0	-0.0075±0.0074	$2.9 \cdot 10^{-10} \pm 7.5 \cdot 10^{-9}$	$-1.4 \cdot 10^{-6} \pm 5.2 \cdot 10^{-6}$	$9.6 \cdot 10^{-8} \pm 4.9 \cdot 10^{-4}$
5	3.1±0.6	-1.5±0.7	1.2±1.5	3.0±5.6
10	0.2±1.7	1.4±0.7	0.078±0.33	6.7±7.9
15	13.0±5.4	3.2±1.6	13.0±7.4	5.0±26.1
20	23.2±6.4	16.1±3.0	19.4±9.9	10.6±7.8

Table S IV: Time to peak fractional variation of calcium transient relative to initial value measured in mice ventricular cardiomyocytes

Time (min)	Vehicle (mean±s.e.m.) n=18	TTR (mean±s.e.m.) n=13	TTR-ol (mean±s.e.m.) n=14	TTR-fib (mean±s.e.m.) n=19
0	$9.7 \cdot 10^{-7} \pm 1.2 \cdot 10^{-6}$	$1.5 \cdot 10^{-6} \pm 1.5 \cdot 10^{-6}$	$1.9 \cdot 10^{-7} \pm 1.1 \cdot 10^{-6}$	$4.7 \cdot 10^{-7} \pm 9.6 \cdot 10^{-7}$
5	23.3±13.5	10.9±7.7	11.4±3.5	6.7±3.8
10	32.7±18.5	15.8±6.5	19.7±10.9	8.6±7.1
15	85.6±52.8	26.8±12.8	60.3±10.2	60.0±6.7
20	225.8±83.1	189.2± 26.3	166.3±16.7	150.73±12.4

Table S V: 50% decay time fractional variation of calcium transient relative to initial value in mice ventricular cardiomyocytes

Time (min)	Vehicle (mean±s.e.m.) n=18	TTR (mean±s.e.m.) n=13	TTR-ol (mean±s.e.m.) n=14	TTR-fib (mean±s.e.m.) n=19
0	$8.3 \cdot 10^{-7} \pm 1.03 \cdot 10^{-6}$	$2.3 \cdot 10^{-7} \pm 4.0 \cdot 10^{-7}$	$3.1 \cdot 10^{-8} \pm 3.3 \cdot 10^{-7}$	$5.9 \cdot 10^{-7} \pm 3.3 \cdot 10^{-7}$
5	14.0±12.6	-2.3±1.6	-3.9±3.0	5.0±2.4
10	17.0±15.3	-7.4±2.8	5.3±5.7	7.4±4.8
15	40.2±23.3	10.6±8.6	16.8±6.1	6.8±4.7
20	202.8±81.4	125.8± 35.1	110.6±25.6	100.4±24.6